

# Molecular Occupancy of Nanodot Arrays

Haogang Cai<sup>1</sup>, Haguy Wolfenson<sup>2</sup>, David Depoil<sup>3</sup>, Michael L. Dustin<sup>3</sup>, Michael P. Sheetz<sup>2</sup>, and  
Shalom J. Wind<sup>4,\*</sup>

*<sup>1</sup>Dept. of Mechanical Engineering, <sup>2</sup>Dept. of Biological Sciences,*

*<sup>4</sup>Dept. of Applied Physics and Applied Mathematics, Columbia University, New York*

*<sup>3</sup>Skirball Institute of Biomolecular Medicine, New York University School of Medicine, New York*

*\*Corresponding author: sw2128@columbia.edu*

## ABSTRACT

Single molecule nanodot arrays, in which a biomolecule of choice (protein, nucleic acid, etc.) is bound to a metallic nanoparticle on a solid substrate, are becoming an increasingly important tool in the study of biomolecular and cellular interactions. We have developed an on-chip measurement protocol to monitor and control the occupancy of nanodot clusters. Arrays of widely spaced nanodots were fabricated on glass surfaces by nanolithography and functionalized with fluorescently-labeled proteins. The molecular occupancy was determined by monitoring individual fluorophore bleaching events, whilst accounting for fluorescence quenching effects. We found that the occupancy depends on nanodot size and binding ligand concentration, which is easily adjusted. The results are scalable with nanodot cluster size, extending to large area close packed arrays. As an example, the nanoarray platform was used to determine the geometric requirement of T-cell activation at the single-molecule level.

Single-molecule nanoarrays, in which individual molecules are presented on a surface, have become an important tool for a broad range of studies and applications, including genomics<sup>1,2</sup>, proteomics<sup>3,4</sup>, protein-DNA interactomics<sup>5,6</sup>, and biodiagnostics<sup>7</sup> based on DNA-DNA<sup>8,9</sup> protein-protein<sup>10</sup>, antigen-antibody<sup>11,12</sup>, or aptamer-protein<sup>13,14</sup> binding. Miniaturization from conventional micro-assays to single-molecule nanoarrays leads to significant improvements in sensitivity, specificity, speed and throughput<sup>15</sup>. Various approaches have been taken to create single-molecule nanoarrays. The most straightforward is the simple deposition from a dilute solution onto bare glass<sup>16,17</sup> or polyethylene glycol (PEG) coated glass<sup>18,19</sup>, relying on the sparse distribution of molecules on the surface to achieve single-molecule resolution. A more sophisticated technique uses zero mode waveguides (ZMWs)<sup>2</sup>, nanoapertures<sup>20</sup> or nanogrids<sup>21</sup>, which restricts the imaging volume, so that, on average, only a single molecular interaction is probed at each site. Nanoarrays with more orderly arrangements have been made by direct patterning of biomolecules by dip-pen nanolithography (DPN)<sup>22-24</sup> or surface chemistry patterning by electron beam lithography (EBL) or nanoimprint lithography (NIL)<sup>25,26</sup>.

A particular type of single-molecule nanoarray that is seeing increasing utility has a biomolecule of choice immobilized on a surface-bound metallic nanoparticle or nanodot, typically ~ 2 – 10 nm in diameter. By tuning the nanodot surface chemistry relative to the background, very high selectivity can be achieved. These nanodot arrays have been finding increasing application in a variety of cellular studies, providing insight into the crucial role of geometric organization of ligands for receptors involved in critical cellular functions, such as adhesion and spreading<sup>27-30</sup>, differentiation<sup>31</sup>, apoptosis<sup>32</sup>, and immune recognition<sup>33-36</sup>.

The basic assumption in the use of these nanoarrays is that each nanodot is occupied by a single molecule (receptor or ligand). This is critical, as the nature of the individual interactions being

probed is generally sensitive to stoichiometry. The small size of the molecules used in these arrays makes this a challenging task, requiring ultra-high resolution techniques to image at the single-molecule level. Transmission electron microscopy (TEM) has been used to directly image protein-bound quantum dots (QDs) on gold nanoparticles of different size created by dip pen nanolithography<sup>37</sup>, showing that the number of bound QDs scales with the nanoparticle size<sup>38</sup>. This sort of measurement requires the use of electron microscopy and is not compatible with surface based nanoarrays, especially in the context of biological experiments. Other strategies based on super-resolution fluorescence microscopy such as photoactivated localization microscopy (PALM) have been applied to gold nanoarrays, but the measured functionalization efficiency in those studies was very low<sup>39</sup>.

In this work, we demonstrate an on-chip technique for determining the molecular occupancy of single-molecule nanoarrays based on the observation of individual fluorescence photobleaching events using common epi-fluorescence microscopy, and we describe how the occupancy can be controlled. The key to the technique is the fabrication of ordered arrays of nanodots spaced apart sufficiently so that the intensity signal and discrete bleaching events from each one can be clearly distinguished. Equally important is highly selective functionalization of the nanodots, in order to minimize the background signal. This approach is based upon our previous work in which we monitored DNA cleavage by a restriction enzyme<sup>5</sup> and single QD blinking events<sup>40</sup> on similar nanoarrays. Here, smaller nanodots in the range of  $\sim 5 - 15$  nm were used so that this platform could be optimized to ensure true single-molecule control. The relationship between the molecular occupancy and factors such as nanodot size and binding ligands concentration were also studied. This is a convenient and effective way to adjust the molecular occupancy for a given nanodot size.

A variety of technologies have been developed to create regular arranged metallic nanoarrays, from bottom-up approach such as block-copolymer micelle nanolithography (BCML)<sup>28,29,31-35,41-44</sup>, and self-assembled nanosphere lithography (NSL)<sup>9-11,45-47</sup>, to top-down approaches, including photolithography<sup>48</sup>, DPN<sup>37,38</sup>, and EBL, NIL<sup>5,27,36,40,49</sup>. The so-called top-down approaches enable heterogeneous arrays on the same surface, with arbitrary geometry and various dot sizes. This is important for the molecular occupancy analysis presented here, because the integration of various patterns on the same sample enables direct comparison between them. Moreover, integration of fixed spacing nanoarrays with other more densely spaced arrays allows for on-chip measurement and calibration.

## RESULTS

### Molecular occupancy measurement by photobleaching

The process for creating the nanoarray platform used in this work is outlined in Supplementary Figure 1. The final step in the process is a thermal anneal of ultra-thin AuPd films at the patterned sites, transforming them into spherical nanoparticles with small diameter and a high degree of uniformity (Fig. 1a). Next, a self-assembled monolayer (SAM) mixture of alkylthiol and biotin-alkylthiol is formed on the nanodots, where the mole fraction could be adjusted. This is followed by passivation of the background unpatterned glass surface with PEG-silane to prevent nonspecific binding and improve the signal-to-background ratio (SBR). For this study, a fluorophore-labeled streptavidin was bound to the biotin in the SAM. We chose streptavidin because it is commonly used to attach a wide variety of molecules to metallic nanoparticles owing to its reliable binding to any moiety that can be biotinylated<sup>5,27,36,40</sup>. The results, however,

can be generalized to other molecular species bound to the nanoparticles, either directly or through a streptavidin (or other molecular) bridge. We developed a molecular model based on protein data bank (PDB) files according to the functionalization process (Fig. 1b). When the nanoarray is under constant exposure to excitation light, the fluorophores bleach over time thus providing a signal for measurement (Fig. 1c).

A typical nanodot array, with an inter-dot spacing of 1  $\mu\text{m}$ , is shown in Fig. 1d. Scanning electron microscopy (SEM) of the mold used to fabricate the nanodot arrays shows both single nanodots and nanodot clusters (Fig. 1d, upper). The atomic force microscopy (AFM) scan in Fig. 1d (lower) shows an example of a AuPd nanoarray with a uniform height profile of  $\sim 7.5$  nm. Since the nanodots are spherical, this is also their lateral size<sup>49</sup>. In order to achieve a sufficiently high SBR, clusters, such as the 1  $\mu\text{m}$ -spaced heptamers interspersed with 10  $\mu\text{m}$ -spaced registration arrays (inset), were used for continuous fluorescence imaging. We used a standard epi-fluorescence microscope with high magnification coupled to an EM-CCD camera that was able to detect single bleaching events. Fig. 1e shows the fluorescence signal from a functionalized nanodot array, where two types of regions of interest (ROIs) are selected: nanodots (inset) and background. By plotting the fluorescence intensity vs. time, and then subtracting the background from the nanodot signal, a typical bleaching curve is obtained, where discrete steps represent bleaching events of individual fluorophores (Fig. 1f). Given the fluorophore/protein (F/P) ratio of the labeled streptavidin, the molecular occupancy could be determined from the number of steps for each site (heptamer, in this case). Since fluorescence is directly proportional to the number of molecules<sup>50</sup>, it is unnecessary to count step numbers for the entire set of bleaching curves for each nanodot or cluster in order to efficiently obtain

statistical results. Eq. (1) gives an alternative way based on the average step size and initial intensity:

$$N = \frac{I}{h \cdot r \cdot c} \quad (1)$$

where  $N$  is the molecular occupancy, i.e. the number of molecules per nanodot;  $I$  is the initial intensity of the nanodot cluster;  $h$  is the bleaching step size;  $r$  is the F/P ratio of the labeled molecule, i.e. the number of fluorophores per molecule (streptavidin in this case); and  $c$  is the cluster size, i.e. the number of nanodots per cluster.

Fig. 1g shows a histogram of step sizes for 7.5 nm nanodots, derived from the bleaching curves (e.g., Fig. 1f); this histogram was fitted to a set of Gaussian distributions. The center of the second peak is approximately twice the value of the first, which indicates simultaneous bleaching events (observed especially in the early stages of the bleaching curves), and must be taken into consideration in determining the average value. Variations in the individual fluorophore intensity are observed, as was shown previously<sup>20,51</sup>. The single-step distribution overlaps the double-step, making it difficult to determine the initial intensity measurement for a small number of fluorophores, as pointed out by Heider et al.<sup>51</sup>. In our case, however, with a sufficiently large number of fluorophores per site ( $r = 3$ ,  $c = 7$ ) and a large sample size ( $n > 1500$ ), the initial intensity measurement using an average step size still provides reliable statistical results.

### **Quenching effect and surface passivation**

It is well known that the fluorescence from a molecule in close proximity to a metal nanoparticle is affected by radiative and nonradiative energy transfer, leading to excited-state enhancement or quenching<sup>52,53</sup>. Recently, both theoretical and experimental works have determined that the fluorescence quenching efficiency increases with the gold nanoparticle size in the range of our

interest<sup>54</sup>. A size-dependent nanometal surface energy transfer (NSET) model was developed by Breshike et al.<sup>55</sup> to explain the dependence of quenching efficiency on both distance and nanodot size. Fig. 1h shows typical bleaching curves and the average step sizes for nanodots with diameters up to 15 nm. The reduction of the step size is consistent with this quenching model. The quenching effect contributes to the variation of individual fluorophore intensity (bleaching step size), as it depends on the distance between the fluorophore and the nanodot surface (Supplementary Fig. 2a, b).

Also shown in Fig. 1h is the step size for nonspecifically bound fluorophores on the background, which is much larger than for the nanodots because of the absence of quenching. In light of this, control of nonspecific binding on the glass substrate (i.e., noise) is critical for these measurements. PEG passivation is widely used in single-molecule studies, but it is typically most effective at low (nanomolar) concentrations<sup>56</sup>, which is suitable for deposition from a dilute solution (20-100 pM<sup>18</sup>). Single-molecule nanoparticle nanoarrays, on the other hand, require a much higher concentration (50 nM<sup>38</sup>-10  $\mu$ M<sup>27</sup>) to ensure functionalization efficiency. Alternatives have been proposed to improve the passivation, such as chlorine-terminated surface<sup>57</sup> and multi-arm PEG<sup>58</sup>, as well as dichlorodimethylsilane (DDS)-Tween-20, which were found to reduce nonspecific adsorption by 5- to 30-fold for a variety of biomolecules<sup>56</sup>. We have found that spin-coating hydrogen silsesquioxane (HSQ) on the glass coverslips, followed by thermal conversion to SiO<sub>2</sub><sup>59</sup>, prior to PEG-silane passivation, is highly effective in increasing the SBR. The 15 nm-thick layer of cured HSQ covers common impurities found on glass coverslip surfaces, thereby reducing the number and size of defective regions in the PEG passivation layer. As a result, the nonspecific bound streptavidin density drops nearly 20-fold to

$0.42 \pm 0.08$  molecules per  $\mu\text{m}^2$  (Supplementary Fig. 3, 4a), ensuring not only sufficient SBR for 1  $\mu\text{m}$ -spaced nanoarrays, but also biological inertness for most applications.

### **Factors affecting molecular occupancy**

Fig. 2a shows an example of a heterogeneous array with nanodots ranging from 7.5 to 17.5 nm. Its fluorescence intensity profile indicates the dependence of molecular occupancy on nanodot size (Fig. 2b). A statistical analysis based on Eq. (1) indicates that the occupancy increases with both the nanodot size and the biotin-alkylthiol concentration (Fig. 2c). This could serve as a guide for the functionalization of nanodot arrays using streptavidin-biotin binding. It introduces a degree of flexibility and alleviates the need to produce nanodots at the same size as the molecule in order to achieve single-molecule occupancy with a pure SAM of biotin-alkylthiol (mole fraction 100%)<sup>38</sup>. Instead, nanodots with a diameter of 7.5 or 12.5 nm at a mole fraction of 50% or 25%, respectively, could also yield single-molecule occupancy, albeit with increased dispersion (see the error bars in Fig. 2c).

The average molecular occupancy appears to scale approximately linearly with the mole fraction of the biotin-alkylthiol SAM (Fig. 2c). This is reasonable, because a higher biotin concentration in the SAM leads to a higher probability of streptavidin binding. The size dependence can be interpreted simply as a packing problem. With the nanodots surrounded by the PEG passivation, which is designed to repel proteins, the streptavidins will tend to bind only when they are within the projected area of a nanodot on the surface plane. Given that streptavidin is close in size to the nanodots in the range of interest<sup>60</sup>, this packing problem can be considered as "circles packing in a circle"<sup>61</sup> rather than "circles packing on a sphere"<sup>62</sup>. Optimal packing numbers of 5 nm-diameter circles in the nanodot projected circles are plotted in Fig. 2d, whose trend line shows



good agreement with the molecular occupancy normalized by the mole fraction. Thus, the molecular occupancy can be estimated by an empirical equation:

$$N = x \cdot p(d, D) \quad (2)$$

where  $x$  is the mole fraction of binding ligands in the mixed SAM,  $d$  is the diameter of the target molecule which binds to the ligands,  $D$  is the diameter of the nanodot, and  $p(d, D)$  is the optimal packing number of circles of diameter  $d$  in a circle of diameter  $D$ . This estimation may be generalized for other functionalization schemes using a mixed SAM. Eq. 2 can also be used to predict the mole fraction  $x$  required to achieve a single-molecule occupancy for a given nanodot size.

### **Scalability and single nanodot/molecule array**

The results presented up to this point were obtained on arrays of heptameric clusters, as in the inset of Fig. 1d. In order to verify its scalability for different cluster sizes, we created a heterogeneous array with clusters containing 1 - 19 nanodots with a diameter of 12.5 nm (Fig. 3a). A biotin fraction of 25% was used to achieve approximately single molecule occupancy on each nanodot, as per Fig. 2c. A profile of the fluorescence image shows that the intensity increases essentially monotonically with cluster size (Fig. 3b). The nanodots in each cluster were in hexagonal arrangement with 60 nm spacing, which is robust in fabrication and ensures that the fluorescence is not quenched by adjacent nanodots. However, the fluorescence intensity is not necessarily uniform across a given 60 nm-spaced cluster (see Supplementary Fig. 5). Therefore, a spatial correction based on the measured point-spread function (PSF) and 1D approximation was applied (Supplementary Table 1). The corrected measurement leads to an average molecular

occupancy per cluster that scales approximately linearly with the cluster size (Fig. 3c) and is in good agreement with a single molecule per nanodot for all cluster sizes.

For the smaller clusters ( $c \leq 4$ ), the signal was quite low, and the SBR was  $\lesssim 1$ . This is insufficient for reliable statistics and is also why heptamers were chosen for the analysis, rather than a single nanodot, particularly in the presence of quenching effect. Despite this, the fluorophore occupancy histogram for a single dot array (Fig. 3d) was analyzed in addition to a heptamer array (Fig. 3e). The molecular occupancy (inset) was obtained by the probability of multiple Gaussian fit, based on the binomial distribution of fluorophores on each streptavidin molecule, which was verified by nonspecific bound streptavidin on the background (Supplementary Fig. 3d). This analysis demonstrated that with an average molecular occupancy of  $\sim 0.9$ , nearly 60% of the single nanodots had one bound molecule, nearly 20% had two bound molecules, and  $> 20\%$  unbound. The actual functionalization efficiency may be higher, considering initial bleaching that might not have been captured in the videos. The molecular occupancy distribution per heptamer  $P_{c=7}$  is in good agreement with the 7th convolution power of the single dot distribution  $P_{c=1}^{*7}$ , which further confirms the scalability of our platform.

### **T-cell stimulation by single-molecule nanoarrays**

We used our nanodot array platform to determine the minimum geometric requirements for T-cell stimulation. The T-cell receptor (TCR) is a relatively small molecule (it is a heterodimer with two  $\sim 40 - 50$  kD chains<sup>63</sup>), and thus controlling the molecular occupancy of antigens-bound nanodots is critical to accurately assessing the spatial and/or density threshold for activation. For these experiments, we used a biotinylated UCHT1 Fab' (a single binding site of TCR) on the streptavidin linker. The surrounding surface was functionalized with a his-tag ICAM-1 linked to

a PEG-silane via a nickel-NTA bridge to facilitate binding of LFA-1, which enhances cell adhesion<sup>36</sup>. A live T-cell on this bifunctional surface is shown in Fig. 4a. Bleaching analysis of 1  $\mu\text{m}$ -spaced heptamer arrays revealed that nanodots ( $D = 7.5 \text{ nm}$ ,  $x = 50\%$ ) had a Fab' occupancy of  $\sim 1$  ( $N_{\text{streptavidin}} = 0.92 \pm 0.28$ ;  $N_{\text{Fab'}}$  =  $0.98 \pm 0.58$ , Supplementary Fig. 6), albeit with a higher coefficient of variation (CV) than streptavidin (Fig. 4b, inset). Although the streptavidin has 3 binding pockets available for the Fab', the actual binding may be limited by the streptavidin orientation on the nanodots and/or possible interactions between Fab' molecules. We have already shown that the molecular occupancy is scalable to larger cluster sizes (Fig. 3c), and indeed, we find the fluorescence intensity of both streptavidin and Fab' to be linear with the nanodot density, as shown in Fig. 4b. This is especially useful for cellular assays, which frequently utilize dense patterns such as extended hexagonal arrays (Supplementary Fig. 7a).

Primary human  $\text{CD4}^+$  T-cell response to the nanoarrays was assessed by monitoring the phosphotyrosine (pY) intensity using total internal reflection fluorescence microscopy (TIRF) 5 minutes after plating. For hexagonal arrays with different spacing from 60 to 300 nm, the average pY intensity decreased with increasing spacing to a threshold  $\sim 100 \text{ nm}$  spacing (corresponding to a density of  $\sim 115 \text{ TCR binding sites per } \mu\text{m}^2$ ), at which point the signal drops to nearly that of cells on the PEG passivation background (outside the pattern area, a negative control) (Fig. 4c). This trend is similar to that reported previously<sup>33-35</sup>, but verified single binding sites with refined spacing ranges result in a more accurate threshold (see Supplementary Table 2). The variation among different platforms is not observed in integrin mediated adhesion, probably because the larger size of the extracellular head of the integrin<sup>27-30</sup>, as discussed in the Supplementary Information.

In addition to hexagonal arrays, our platform also included cluster arrays, which allowed us to decouple the effects of local inter-dot spacing and global density (Fig. 4d). This is not generally doable with arrays made by BCML. Heptamer arrays at a constant density of  $50/\mu\text{m}^2$ , but with spacings ranging from 60 to 90 nm (Supplementary Fig. 7b) showed a negative response (i.e., pY signal equal to the negative control), as shown in Fig. 4d, implying that in the absence of costimulatory and other factors, it is global density, and not local spacing that determines TCR stimulation, with a threshold  $\sim 115$  TCR binding sites per  $\mu\text{m}^2$ . This requirement is much higher than stimulation by antigen presenting cells (APCs)<sup>64</sup> or artificial APC surfaces<sup>21</sup>. We speculate that in the absence of sufficient ICAM-1 density (which was  $< 50/\mu\text{m}^2$  in our experiments, due to a low grafting yield of nitrilotriacetic acid (NTA) on the PEG background), the TCR must serve a dual role of antigen recognition and adhesion receptor, which requires additional TCR molecules. Meanwhile, 60 nm heptamer arrays at a global density from 100 to  $250/\mu\text{m}^2$  (Supplementary Fig. 7c) had a lower response than hexagonal arrays, suggesting a secondary effect of local spacing.

## CONCLUSION

We have developed a technique to determine the molecular occupancy of metallic nanodot arrays by observing discrete steps in the intensity time profiles, which represent individual fluorophore bleaching events. The technique takes into account both the nanodot size and the binding ligand concentration, and it also accounts for quenching effects. The technique employs conventional epi-fluorescence microscopy and is compatible with on-chip, in situ measurement, so that it can be incorporated into real single-molecule experiments. A thin layer of thermally cured HSQ

before conventional PEG-silane passivation reduced the background noise of nonspecific binding by nearly 20-fold and improved the SBR effectively.

For streptavidins on AuPd nanodots ranging from 5 to 15 nm, the histogram of occupancy was obtained for different mole fraction of biotin-alkylthiol. Nanodots with a diameter of 7.5 or 12.5 nm at mole fractions of 50% or 25% will yield single-molecule occupancy respectively. The results are scalable for various cluster sizes and can be reasonably extended to dense close packed arrays. Since the binding ligand concentration of the mixed SAM can be easily adjusted, it introduces great flexibility in creating single-molecule array. This was demonstrated by, but is not limited to, streptavidin-biotin binding, and can be adapted to other functionalization strategies using a mixed SAM. Photobleaching analysis is also a general method for the on-chip measurement of molecular occupancy on nanodot arrays.

Finally, single-molecule occupancy was demonstrated to be crucial to improving the accuracy of cellular assays. Our platform also provides arbitrary geometries and better comparison between different patterns on a same chip. A density threshold of  $\sim 115$  TCR binding sites per  $\mu\text{m}^2$  has been determined for human T-cell stimulation (with low ICAM-1 concentration), possibly because the TCR has to play dual roles of both immune activity and adhesion. Overall, nanoscale geometric organization affects T-cell activation and behavior, which has potential applications in adoptive immunotherapy. Further investigation would require an improved presentation of ICAM-1, in order to better mimic the APC surface.

## **METHODS**

### **Nanodot fabrication**

AuPd nanodot arrays were fabricated on standard glass coverslips (22 × 22 mm, no. 1.5, Corning) using EBL or NIL, with self-aligned pattern transfer<sup>36,49</sup>, which is shown schematically in Supplementary Fig. 1a. In brief, PMMA (MW 495K, Microchem) was patterned by direct EBL (NanoBeam nB5), with a thin conductive layer of Aquasave, which was rinsed by DI water before development in MIBK/IPA 3:1 at 4 °C and ultrasonication for 1min. Alternatively, PMMA (MW 35K, Micro Resist Technology) was used for thermal NIL (Nanonex BX-200) at 500 psi and 180° C for 5 min, in order to improve the throughput. NIL templates were made of ~ 25 nm HSQ (Dow Corning XR-1541) on Si substrate, developed in MF-CD-26 for 4 min, then annealed on hotplate at 540° C for 1 hr, followed by anti-adhesion coating (Nanonex Ultra-100). In both cases, the PMMA thickness was ~ 60 nm. After lithography, a 12 nm Ti hard mask was evaporated (Semicore SC2000) at an angle of 30°, which protects the thin PMMA layer in oxygen plasma (Oxford PlasmaLab 80), exposing only the nanodot regions. AuPd (60/40) with Ti adhesion layer was evaporated at a rate of 0.1 Å/s, forming nanodot arrays after lift-off in boiling acetone for 5 min. An annealing step at 540° C for 2 hrs caused the nanodots to agglomerate into spheres whose size was coded by the lithography. In order to reduce the background noise caused by nonspecific binding, a 15 nm HSQ layer was spun on the glass coverslips and thermally cured at 540° C for 2 hrs before the nanoarray fabrication.

### **Functionalization**

The functionalization process is shown in Supplementary Fig. 1b. First of all, nanoarray samples were cleaned by immersion in 1.5 hr-aged piranha solution (3:1 H<sub>2</sub>SO<sub>4</sub>:H<sub>2</sub>O<sub>2</sub>) for 3 min,

followed by exposure to an oxygen plasma for 5 min. This process also activates the glass surface for binding of PEG-silane by creating hydroxyl groups. Samples were immediately immersed in a freshly prepared 1 mM mixture of HS-C<sub>11</sub>-EG<sub>6</sub>-Biotin and HS-C<sub>11</sub>-EG<sub>3</sub>-OH (ProChimia Surfaces) solution in ethanol for ~ 18 hr (overnight). The biotin concentration on the SAM formed on AuPd nanodots was thereby adjusted by the mole fraction of biotin-alkylthiol. The thiolated samples were rinsed by ethanol, dried and then incubated in a solution of 2 mg mPEG-Silane (MW5000, Laysan Bio) in 25 mL anhydrous toluene with 30 µL acetic acid (as a catalyst) for 48 hrs. The long PEGylation time was found to improve the passivation against nonspecific binding. Samples were rinsed with acetone then ethanol and blew dry. They were incubated for 2 hrs in 10 µg/mL streptavidin (Streptavidin, Alexa Fluor 555 Conjugate, F/P 3:1, Life Technologies) solution in 1.5mL Phosphate-buffered saline (PBS, Gibco DPBS 1×) with 1mg/mL Albumin. In this way, streptavidin molecules bind to AuPd nanodots, whose occupancy can be adjusted by both dot size and mole fraction of biotin-alkylthiol.

In the case of T-cell assays<sup>36</sup>, 1 mg silane-PEG-NHS (MW5000, Nanocs) solution in 25 mL anhydrous methanol with 1 mM NTA-L-lysine was incubated overnight to synthesize silane-PEG-NTA, which was used in place of mPEG-silane. After PEGylation, samples were first incubated in 40 mM aqueous NiSO<sub>4</sub> for 1 hr to adsorb Ni(II) to the NTA groups, followed by 1 µg/mL His-tag ICAM-1 solution in PBS for 2 hrs. Then the samples were incubated in streptavidin solution in PBS for 30 min, followed by 2 µg/mL biotinylated UCHT1 Fab-568 (F/P 0.45) for another 30 min.

## **Microscopy and Cell assays**

Nanoarray samples were mounted in a chamber for replaceable coverslips (CSC-22×22, Bioscience Tools) and covered with buffer solution (PBS). For molecular occupancy of streptavidin-555, the measurements were done by conventional epi-fluorescence microscopy (Olympus IX81) using a DSRed filter for excitation and emission. The nanoarray fluorescence was collected by an oil-immersion objective (100×, 1.49NA, Olympus) with an additional 2× magnification, and recorded by an EM-CCD camera (Cascade II 512, Photometrics) at 50 frames per second for 210 s.

For T-cell assays, primary human CD4<sup>+</sup> cells were plated on the nanoarray surfaces and fixed after 5 min. pY was stained by...

### **Data analysis**

ImageJ was used for image processing and data analysis. Both the signals of nanodot array and the background noises of nonspecific bound fluorophores were detected by the "Mosaic" plug-in, and then separated by a self-written macro according to the nanodot geometric arrangement (Supplementary Fig. 5a). A 3×3 pixel ROI was used for the bleaching analysis. The fluorescence average over the first 1 s exposure was used as the initial intensity. A step detection algorithm for molecular motors<sup>65</sup> was adopted to fit the bleaching curves, so that the total number of step and the size of each step were extracted using Matlab. The histogram of step size with double peaks was fitted by a mixed Gaussian distribution using expectation maximization (EM) algorithm.

With a similar algorithm, a set of single Gaussians ( $n$ th convolution powers) based on the fitted single fluorophore intensity (bleaching step size) distribution was used to fit the continuous histogram of intensity. The resulted discrete probability distribution provided an estimation on the fluorophore occupancy (Supplementary Fig. 3d, 6b), which is better than simply dividing the



intensity histogram by the average bleaching step size. Similarly, a Gaussian approximation to the binomial distribution of the fluorophore number per streptavidin was used to estimate the molecular occupancy (Fig. 3d, e, Supplementary Fig. 3c), which is better than simple division by the F/P ratio.

### **Acknowledgements**

The authors thank Dr. M. Palma for guidance on the single fluorophore bleaching measurements. This work was supported primarily by the National Science Foundation (NSF) under award no. CMMI-1300590 and by the National Institutes of Health (NIH) Common Fund Nanomedicine program grant PN2 EY016586. The authors are grateful to the Columbia Nano Initiative clean room for making the facilities available for this work.

### **Contributions**

HC performed experiments and data analysis and wrote the manuscript. HW performed fluorescence bleaching experiments. DD prepared antibodies and performed T-cell assays. MLD and MPS designed cell assays, analyzed data and participated in preparation of the manuscript. SJW designed the experiments, analyzed data and wrote the manuscript.

### **Competing financial interests**

The authors declare no competing financial interests.

### **Corresponding author**

Correspondence to: Shalom J. Wind

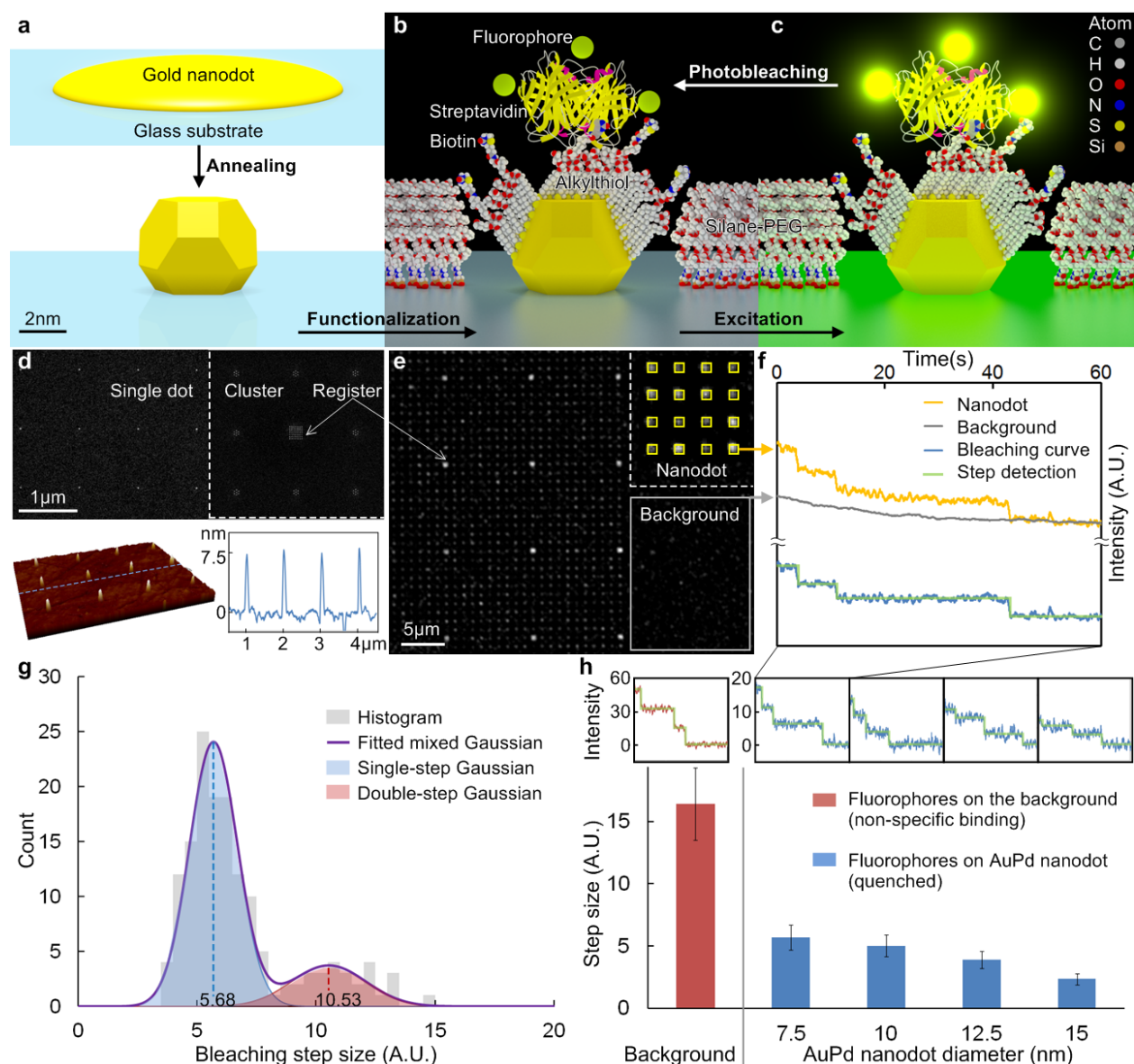


Figure 1. Schematic diagram of the metallic nanodot array: (a) annealing, (b) functionalization, (c) excitation and photobleaching of the fluorophores labeled on a streptavidin (only the SAM in the cross-section is shown for clarity). (d) SEM image of the NIL mold and AFM image of the AuPd nanodot ( $D = 7.5$  nm) array. (e) Fluorescence image with ROIs of both nanodot (heptamer) and background. (f) Fluorescence intensity vs. time. The size of the steps is close, indicating the each step represents the bleaching of a single fluorophore. (g) Bleaching step size histogram of 7.5 nm nanodot. (h) Average bleaching step size vs. AuPd nanodot size.

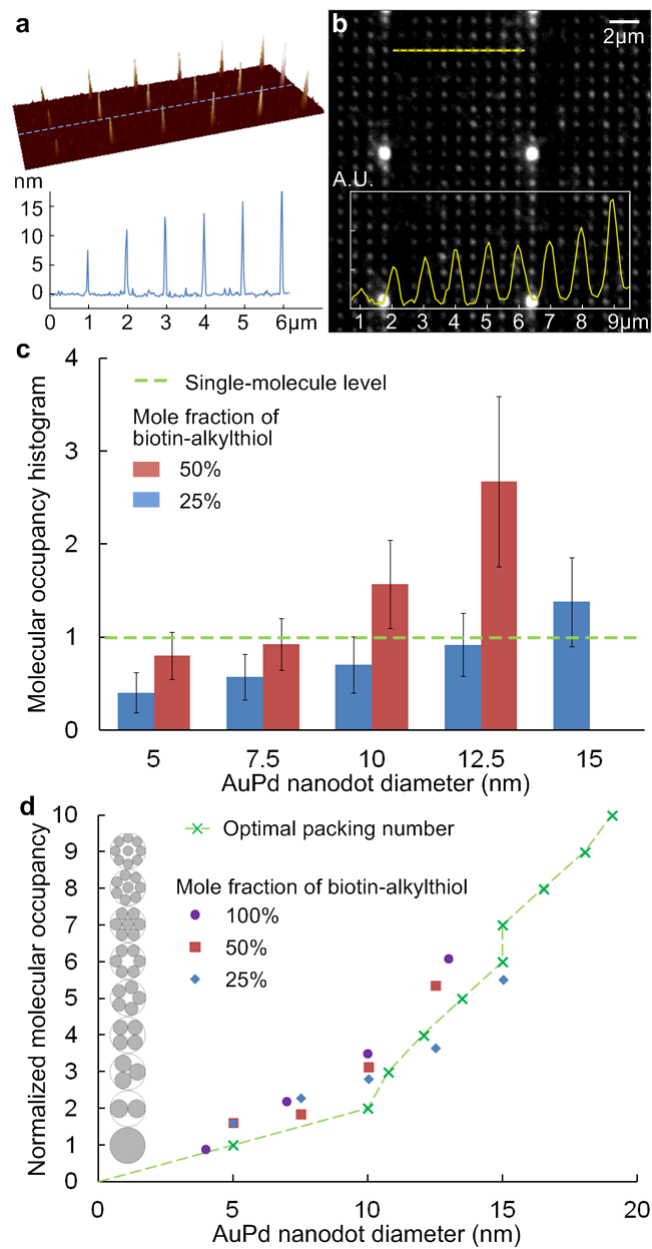


Figure 2. A heterogeneous nanoarray with various dot sizes: (a) AFM image, (b) fluorescence image. (c) Histogram of the average molecular occupancy vs. nanodot size ( $n > 1500$ ). (d) Molecular occupancy normalized by the mole fraction of biotin-alkylthiol. Data for mole fractions of 50% and 25% from Fig. 2c, data for 100% from <sup>38</sup> (Error bars removed for clarity).

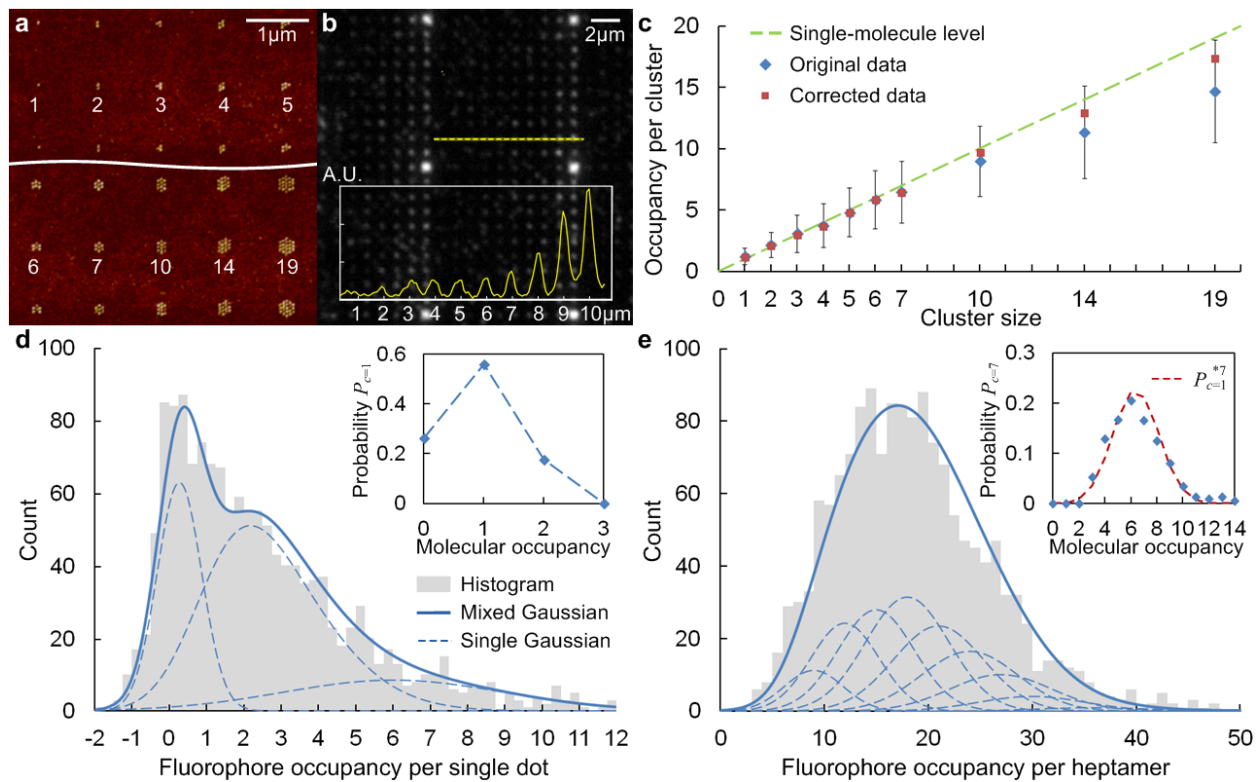


Figure 3. A heterogeneous nanoarray with various cluster sizes: (a) AFM image, (b) fluorescence image. (c) Histogram of the molecular occupancy per cluster vs. cluster size. Fluorophore and molecular occupancy distributions for (d) single dot and (e) heptamer arrays.

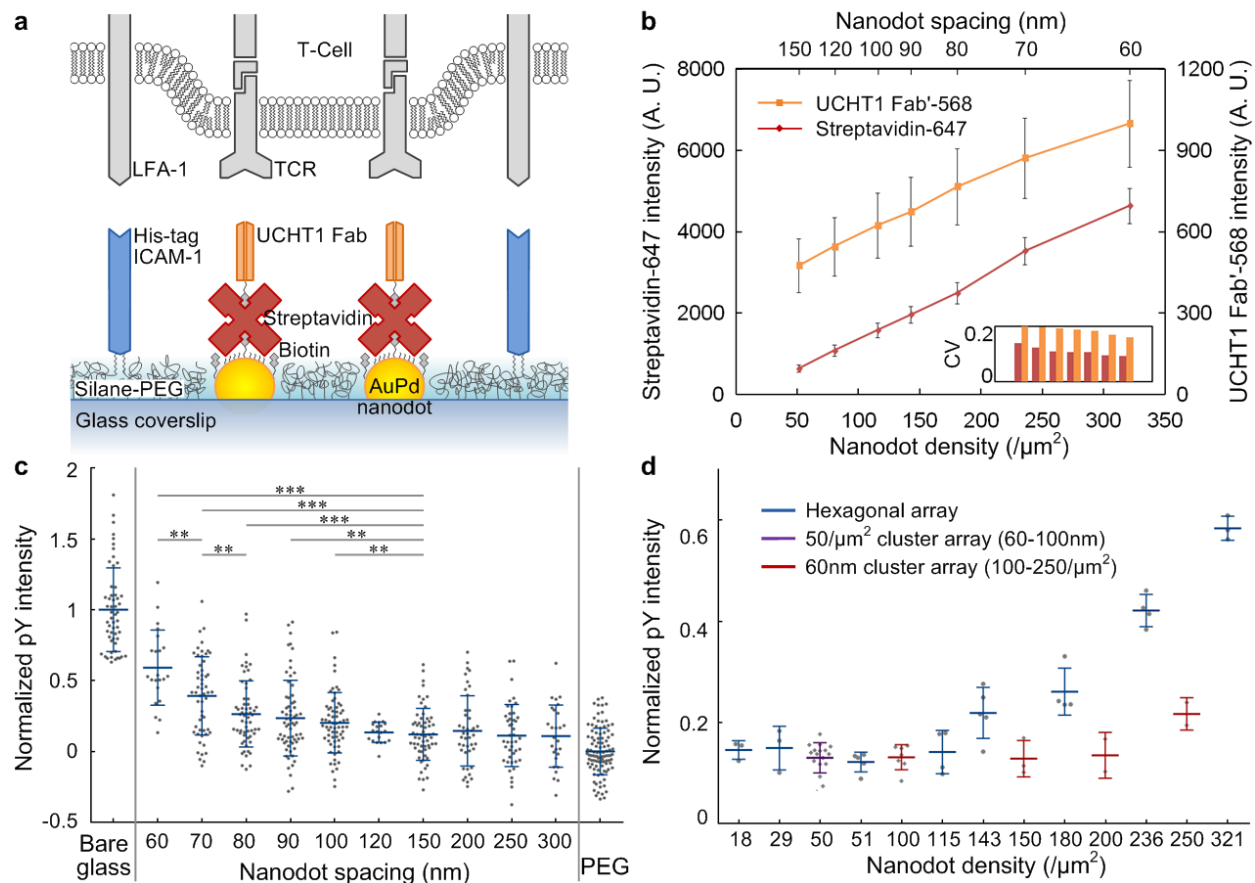


Figure 4. (a) Schematic diagram of the bifunctional nanoarray surface with a live T-cell. (b) Fluorescence intensity of both streptavidin-647 and UCHT1 Fab'-568 for hexagonal arrays with various spacing. Normalized pY intensity after 5 min. stimulation: (c) plot against nanodot spacing, individual cells shown as dots, \*\*\* =  $p < 0.001$ , \*\* =  $p < 0.01$  (Wilcoxon rank sum test), positive control: nonspecific bound Fab' and ICAM-1 on bare glass (maximum concentration), negative control: PEG passivation background without Fab' (minimized concentration). (d) plot against nanodot density, individual experiments shown as dots.

## References

- 1 Drmanac, R. *et al.* Human Genome Sequencing Using Unchained Base Reads on Self-Assembling DNA Nanoarrays. *Science* **327**, 78-81, doi:DOI 10.1126/science.1181498 (2010).
- 2 Eid, J. *et al.* Real-Time DNA Sequencing from Single Polymerase Molecules. *Science* **323**, 133-138, doi:DOI 10.1126/science.1162986 (2009).
- 3 Kingsmore, S. F. Multiplexed protein measurement: technologies and applications of protein and antibody arrays. *Nature Reviews Drug Discovery* **5**, 310-320, doi:DOI 10.1038/nrd2006 (2006).
- 4 Lynch, M. *et al.* Functional protein nanoarrays for biomarker profiling. *Proteomics* **4**, 1695-1702, doi:DOI 10.1002/pmic.200300701 (2004).
- 5 Palma, M. *et al.* Selective Biomolecular Nanoarrays for Parallel Single-Molecule Investigations. *J. Am. Chem. Soc.* **133**, 7656-7659, doi:Doi 10.1021/Ja201031g (2011).
- 6 Bulyk, M. L., Gentalen, E., Lockhart, D. J. & Church, G. M. Quantifying DNA-protein interactions by double-stranded DNA arrays. *Nat. Biotechnol.* **17**, 573-577 (1999).
- 7 Rosi, N. L. & Mirkin, C. A. Nanostructures in biodiagnostics. *Chem. Rev.* **105**, 1547-1562, doi:Doi 10.1021/Cr030067f (2005).
- 8 Taton, T. A., Mirkin, C. A. & Letsinger, R. L. Scanometric DNA array detection with nanoparticle probes. *Science* **289**, 1757-1760, doi:DOI 10.1126/science.289.5485.1757 (2000).
- 9 Li, M. *et al.* Plasmonic Nanorice Antenna on Triangle Nanoarray for Surface-Enhanced Raman Scattering Detection of Hepatitis B Virus DNA. *Anal. Chem.* **85**, 2072-2078, doi:Doi 10.1021/Ac303387a (2013).
- 10 Haes, A. J. & Van Duyne, R. P. A nanoscale optical biosensor: Sensitivity and selectivity of an approach based on the localized surface plasmon resonance spectroscopy of triangular silver nanoparticles. *J. Am. Chem. Soc.* **124**, 10596-10604, doi:DOI 10.1021/ja020393x (2002).
- 11 Haes, A. J., Hall, W. P., Chang, L., Klein, W. L. & Van Duyne, R. P. A localized surface plasmon resonance biosensor: First steps toward an assay for Alzheimer's disease. *Nano Lett.* **4**, 1029-1034, doi:DOI 10.1021/nl049670j (2004).
- 12 Lee, K. B., Kim, E. Y., Mirkin, C. A. & Wolinsky, S. M. The use of nanoarrays for highly sensitive and selective detection of human immunodeficiency virus type 1 in plasma. *Nano Lett.* **4**, 1869-1872, doi:Doi 10.1021/Nl049002y (2004).
- 13 Guo, L. H., Ferhan, A. R., Lee, K. & Kim, D. H. Nanoarray-Based Biomolecular Detection Using Individual Au Nanoparticles with Minimized Localized Surface Plasmon Resonance Variations. *Anal. Chem.* **83**, 2605-2612, doi:DOI 10.1021/ac200432c (2011).
- 14 McCauley, T. G., Hamaguchi, N. & Stanton, M. Aptamer-based biosensor arrays for detection and quantification of biological macromolecules. *Anal. Biochem.* **319**, 244-250, doi:Doi 10.1016/S0003-2697(03)00297-5 (2003).
- 15 Wingren, C. & Borrebaeck, C. A. K. Progress in miniaturization of protein arrays - a step closer to high-density nanoarrays. *Drug Discov. Today* **12**, 813-819, doi:DOI 10.1016/j.drudis.2007.08.003 (2007).
- 16 Peterson, E. M. & Harris, J. M. Quantitative Detection of Single Molecules in Fluorescence Microscopy Images. *Anal. Chem.* **82**, 189-196, doi:10.1021/ac901710t (2010).
- 17 Hanley, D. C. & Harris, J. M. Quantitative dosing of surfaces with fluorescent molecules: Characterization of fractional monolayer coverages by counting single molecules. *Anal. Chem.* **73**, 5030-5037, doi:10.1021/ac010572h (2001).
- 18 Roy, R., Hohng, S. & Ha, T. A practical guide to single-molecule FRET. *Nat. Methods* **5**, 507-516, doi:Doi 10.1038/Nmeth.1208 (2008).

- 19 Morimatsu, M., Mekhdjian, A. H., Adhikari, A. S. & Dunn, A. R. Molecular Tension Sensors Report Forces Generated by Single Integrin Molecules in Living Cells. *Nano Lett.* **13**, 3985-3989, doi:DOI 10.1021/nl4005145 (2013).
- 20 Kinz-Thompson, C. D. *et al.* Robustly Passivated, Gold Nanoaperture Arrays for Single-Molecule Fluorescence Microscopy. *Acs Nano* **7**, 8158-8166, doi:Doi 10.1021/Nn403447s (2013).
- 21 Manz, B. N., Jackson, B. L., Petit, R. S., Dustin, M. L. & Groves, J. T-cell triggering thresholds are modulated by the number of antigen within individual T-cell receptor clusters. *Proceedings of the National Academy of Sciences of the United States of America* **108**, 9088-9094, doi:10.1073/pnas.1018771108/-/DCSupplemental (2011).
- 22 Nam, J. M. *et al.* Bioactive protein nanoarrays on nickel oxide surfaces formed by dip-pen nanolithography. *Angew Chem Int Edit* **43**, 1246-1249, doi:DOI 10.1002/anie.200353203 (2004).
- 23 Lee, K. B., Park, S. J., Mirkin, C. A., Smith, J. C. & Mrksich, M. Protein nanoarrays generated by dip-pen nanolithography. *Science* **295**, 1702-1705, doi:DOI 10.1126/science.1067172 (2002).
- 24 Demers, L. M. *et al.* Direct patterning of modified oligonucleotides on metals and insulators by dip-pen nanolithography. *Science* **296**, 1836-1838, doi:DOI 10.1126/science.1071480 (2002).
- 25 Gopinath, A. & Rothmund, P. W. K. Optimized Assembly and Covalent Coupling of Single-Molecule DNA Origami Nano arrays. *Acs Nano* **8**, 12030-12040, doi:DOI 10.1021/nn506014s (2014).
- 26 Hoff, J. D., Cheng, L. J., Meyhofer, E., Guo, L. J. & Hunt, A. J. Nanoscale protein patterning by imprint lithography. *Nano Lett.* **4**, 853-857, doi:DOI 10.1021/nl049758x (2004).
- 27 Schvartzman, M. *et al.* Nanolithographic control of the spatial organization of cellular adhesion receptors at the single-molecule level. *Nano Lett* **11**, 1306-1312, doi:10.1021/nl104378f (2011).
- 28 Arnold, M. *et al.* Activation of integrin function by nanopatterned adhesive interfaces. *Chemphyschem* **5**, 383-388, doi:DOI 10.1002/cphc.200301014 (2004).
- 29 Cavalcanti-Adam, E. A. *et al.* Cell spreading and focal adhesion dynamics are regulated by spacing of integrin ligands. *Biophys. J.* **92**, 2964-2974, doi:DOI 10.1529/biophysj.106.089730 (2007).
- 30 Huang, J. H. *et al.* Impact of Order and Disorder in RGD Nanopatterns on Cell Adhesion. *Nano Lett.* **9**, 1111-1116, doi:Doi 10.1021/Nl803548b (2009).
- 31 Jaehrlich, S., Thelen, K., Wolfram, T. & Pollerberg, G. E. Nanopatterns Biofunctionalized with Cell Adhesion Molecule DM-GRASP Offered as Cell Substrate: Spacing Determines Attachment and Differentiation of Neurons. *Nano Lett.* **9**, 4115-4121, doi:DOI 10.1021/nl9023325 (2009).
- 32 Ranzinger, J. *et al.* Nanoscale Arrangement of Apoptotic Ligands Reveals a Demand for a Minimal Lateral Distance for Efficient Death Receptor Activation. *Nano Lett.* **9**, 4240-4245, doi:DOI 10.1021/nl902429b (2009).
- 33 Deeg, J. *et al.* T cell activation is determined by the number of presented antigens. *Nano Lett* **13**, 5619-5626, doi:10.1021/nl403266t (2013).
- 34 Matic, J., Deeg, J., Scheffold, A., Goldstein, I. & Spatz, J. P. Fine Tuning and Efficient T Cell Activation with Stimulatory aCD3 Nanoarrays. *Nano Lett.* **13**, 5090-5097, doi:Doi 10.1021/Nl4022623 (2013).
- 35 Delcassian, D. *et al.* Nanoscale Ligand Spacing Influences Receptor Triggering in T Cells and NK Cells. *Nano Lett.* **13**, 5608-5614, doi:Doi 10.1021/Nl403252x (2013).
- 36 Cai, H. *et al.* Bifunctional nanoarrays for probing the immune response at the single-molecule level. *Journal of vacuum science and technology. B, Nanotechnology & microelectronics : materials, processing, measurement, & phenomena : JVST B* **31**, 6F902, doi:10.1116/1.4823764 (2013).

- 37 Chai, J. A. *et al.* Scanning probe block copolymer lithography. *Proceedings of the National Academy of Sciences of the United States of America* **107**, 20202-20206, doi:DOI 10.1073/pnas.1014892107 (2010).
- 38 Chai, J. A., Wong, L. S., Giam, L. & Mirkin, C. A. Single-molecule protein arrays enabled by scanning probe block copolymer lithography. *Proceedings of the National Academy of Sciences of the United States of America* **108**, 19521-19525, doi:DOI 10.1073/pnas.1116099108 (2011).
- 39 Lohmuller, T. *et al.* Supported membranes embedded with fixed arrays of gold nanoparticles. *Nano Lett* **11**, 4912-4918, doi:10.1021/nl202847t (2011).
- 40 Abramson, J., Palma, M., Wind, S. J. & Hone, J. Quantum dot nanoarrays: self-assembly with single-particle control and resolution. *Adv. Mater.* **24**, 2207-2211, doi:10.1002/adma.201104216 (2012).
- 41 Aydin, D. *et al.* Micro-Nanostructured Protein Arrays: A Tool for Geometrically Controlled Ligand Presentation. *Small* **5**, 1014-1018, doi:DOI 10.1002/smll.200801219 (2009).
- 42 Glass, R. *et al.* Micro-nanostructured interfaces fabricated by the use of inorganic block copolymer micellar monolayers as negative resist for electron-beam lithography. *Adv. Funct. Mater.* **13**, 569-575 (2003).
- 43 Glass, R., Möller, M. & Spatz, J. P. Block copolymer micelle nanolithography. *Nanotechnology* **14**, 1153-1160 (2003).
- 44 Spatz, J. P. *et al.* Ordered deposition of inorganic clusters from micellar block copolymer films. *Langmuir : the ACS journal of surfaces and colloids* **16**, 407-415, doi:Doi 10.1021/La990070n (2000).
- 45 Anker, J. N. *et al.* Biosensing with plasmonic nanosensors. *Nat Mater* **7**, 442-453, doi:DOI 10.1038/nmat2162 (2008).
- 46 Haynes, C. L. & Van Duyne, R. P. Nanosphere lithography: A versatile nanofabrication tool for studies of size-dependent nanoparticle optics. *J. Phys. Chem. B* **105**, 5599-5611, doi:DOI 10.1021/jp010657m (2001).
- 47 Hulsteen, J. C. & Vanduyne, R. P. Nanosphere Lithography - a Materials General Fabrication Process for Periodic Particle Array Surfaces. *Journal of Vacuum Science & Technology a-Vacuum Surfaces and Films* **13**, 1553-1558, doi:Doi 10.1116/1.579726 (1995).
- 48 Sun, S. Q. *et al.* Fabrication of gold micro- and nanostructures by photolithographic exposure of thiol-stabilized gold nanoparticles. *Nano Lett.* **6**, 345-350, doi:Doi 10.1021/Nl052130h (2006).
- 49 Schvartzman, M. & Wind, S. J. Robust pattern transfer of nanoimprinted features for sub-5-nm fabrication. *Nano Lett* **9**, 3629-3634, doi:10.1021/nl9018512 (2009).
- 50 Qian, H. & Elson, E. L. Distribution of Molecular Aggregation by Analysis of Fluctuation Moments. *Proceedings of the National Academy of Sciences of the United States of America* **87**, 5479-5483, doi:DOI 10.1073/pnas.87.14.5479 (1990).
- 51 Heider, E. C., Peterson, E. M., Barhoum, M., Gericke, K. H. & Harris, J. M. Quantitative Fluorescence Microscopy To Determine Molecular Occupancy of Phospholipid Vesicles. *Anal. Chem.* **83**, 5128-5136, doi:DOI 10.1021/ac200129n (2011).
- 52 Holzmeister, P. *et al.* Quantum yield and excitation rate of single molecules close to metallic nanostructures. *Nat Commun* **5**, doi:ARTN 5356  
DOI 10.1038/ncomms6356 (2014).
- 53 Dulkeith, E. *et al.* Fluorescence quenching of dye molecules near gold nanoparticles: Radiative and nonradiative effects. *Phys. Rev. Lett.* **89**, doi:Artn 203002  
Doi 10.1103/Physrevlett.89.203002 (2002).



- 54 Chhabra, R. *et al.* Distance-dependent interactions between gold nanoparticles and fluorescent molecules with DNA as tunable spacers. *Nanotechnology* **20**, doi:Artn 485201  
Doi 10.1088/0957-4484/20/48/485201 (2009).
- 55 Breshike, C. J., Riskowski, R. A. & Strouse, G. F. Leaving Forster Resonance Energy Transfer Behind: Nanometal Surface Energy Transfer Predicts the Size-Enhanced Energy Coupling between a Metal Nanoparticle and an Emitting Dipole. *J Phys Chem C* **117**, 23942-23949, doi:Doi 10.1021/Jp407259r (2013).
- 56 Hua, B. Y. *et al.* An improved surface passivation method for single-molecule studies. *Nat. Methods* **11**, 1233+, doi:Doi 10.1038/Nmeth.3143 (2014).
- 57 Zhu, X. Y. *et al.* Grafting of high-density poly(ethylene glycol) monolayers on Si(111). *Langmuir : the ACS journal of surfaces and colloids* **17**, 7798-7803, doi:DOI 10.1021/la010672i (2001).
- 58 Cha, T., Guo, A., Jun, Y., Pei, D. Q. & Zhu, X. Y. Immobilization of oriented protein molecules on poly(ethylene glycol)-coated Si(111). *Proteomics* **4**, 1965-1976, doi:10.1002/pmic.200300747 (2004).
- 59 Liou, H. C. & Pretzer, J. Effect of curing temperature on the mechanical properties of hydrogen silsesquioxane thin films. *Thin Solid Films* **335**, 186-191, doi:Doi 10.1016/S0040-6090(98)00881-5 (1998).
- 60 molecular models, as well as measurements by Neish et al using AFM and Cooper et al using scanning tunneling microscopy (STM) indicate a dimension of ~5 nm.
- 61 Graham, R. L., Lubachevsky, B. D., Nurmela, K. J. & Ostergard, P. R. J. Dense packings of congruent circles in a circle. *Discrete Math* **181**, 139-154, doi:Doi 10.1016/S0012-365x(97)00050-2 (1998).
- 62 Clare, B. W. & Kepert, D. L. The Optimal Packing of Circles on a Sphere. *J. Math. Chem.* **6**, 325-349, doi:Doi 10.1007/Bf01192589 (1991).
- 63 Weiss, A. Structure and Function of the T-Cell Antigen Receptor. *J. Clin. Invest.* **86**, 1015-1022, doi:Doi 10.1172/Jci114803 (1990).
- 64 Irvine, D. J., Purbhoo, M. A., Krogsgaard, M. & Davis, M. M. Direct observation of ligand recognition by T cells. *Nature* **419**, 845-849 (2002).
- 65 Aggarwal, T., Materassi, D., Davison, R., Hays, T. & Salapaka, M. Detection of Steps in Single Molecule Data. *Cell Mol Bioeng* **5**, 14-31, doi:DOI 10.1007/s12195-011-0188-5 (2012).

## 1. Fabrication and functionalization

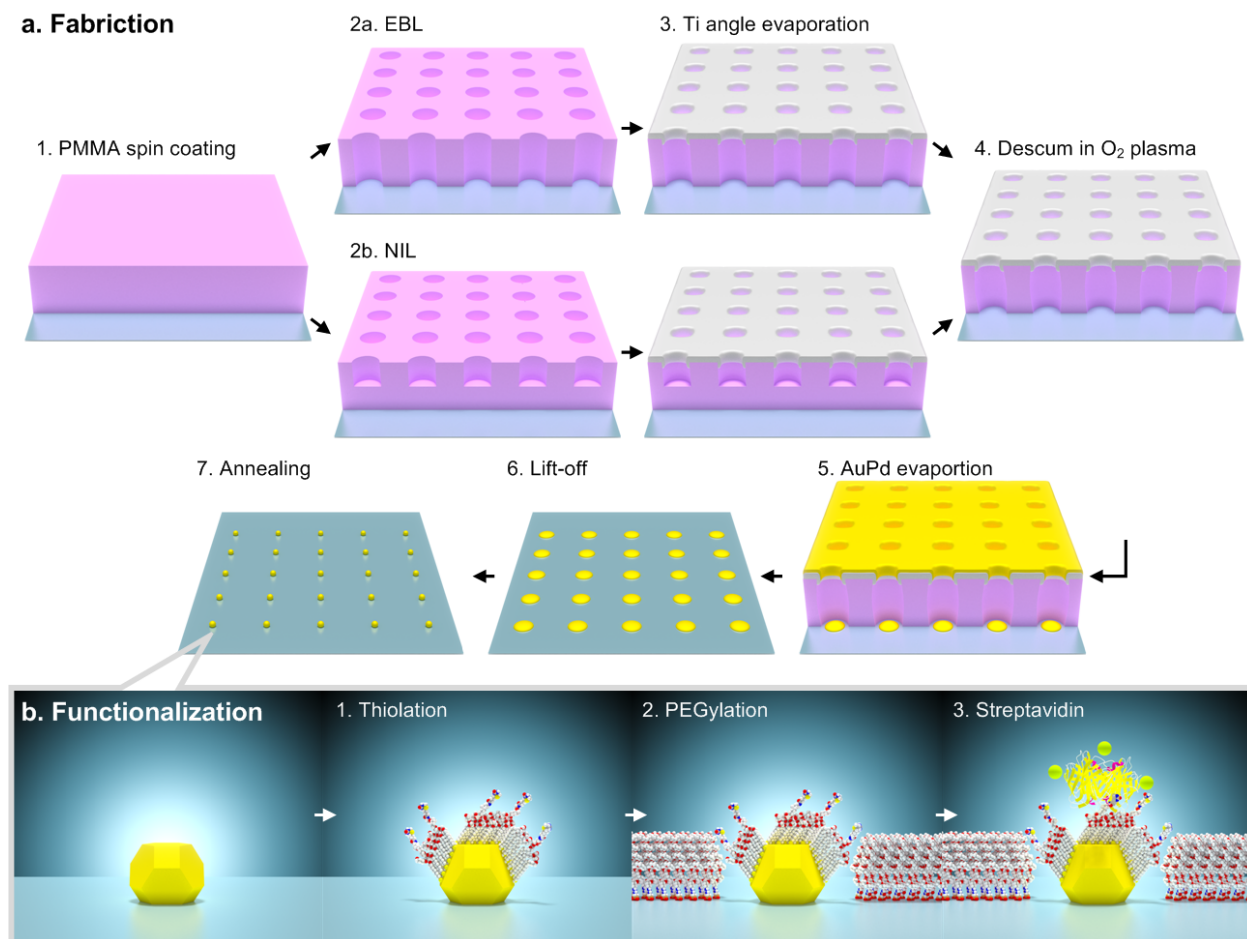


Figure 1. (a) Fabrication and (b) functionalization of AuPd nanoarrays.

Whereas gold is the most commonly used material for bio-conjugated nanoparticles, exploiting the covalent thiolate linkage to various terminal groups for further functionalization<sup>1</sup>, an AuPd alloy (60/40) was used in this work, because it is more compatible with our self-aligned nanodot fabrication scheme (Fig. 1a) due to its smaller grain size than Au, which allows it to agglomerate into a single particle at each site. Stable self-assembled monolayers (SAMs) with thiol end groups form on AuPd<sup>2</sup> as well as on Pd<sup>3</sup>.

## 2. Molecular model and quenching effect

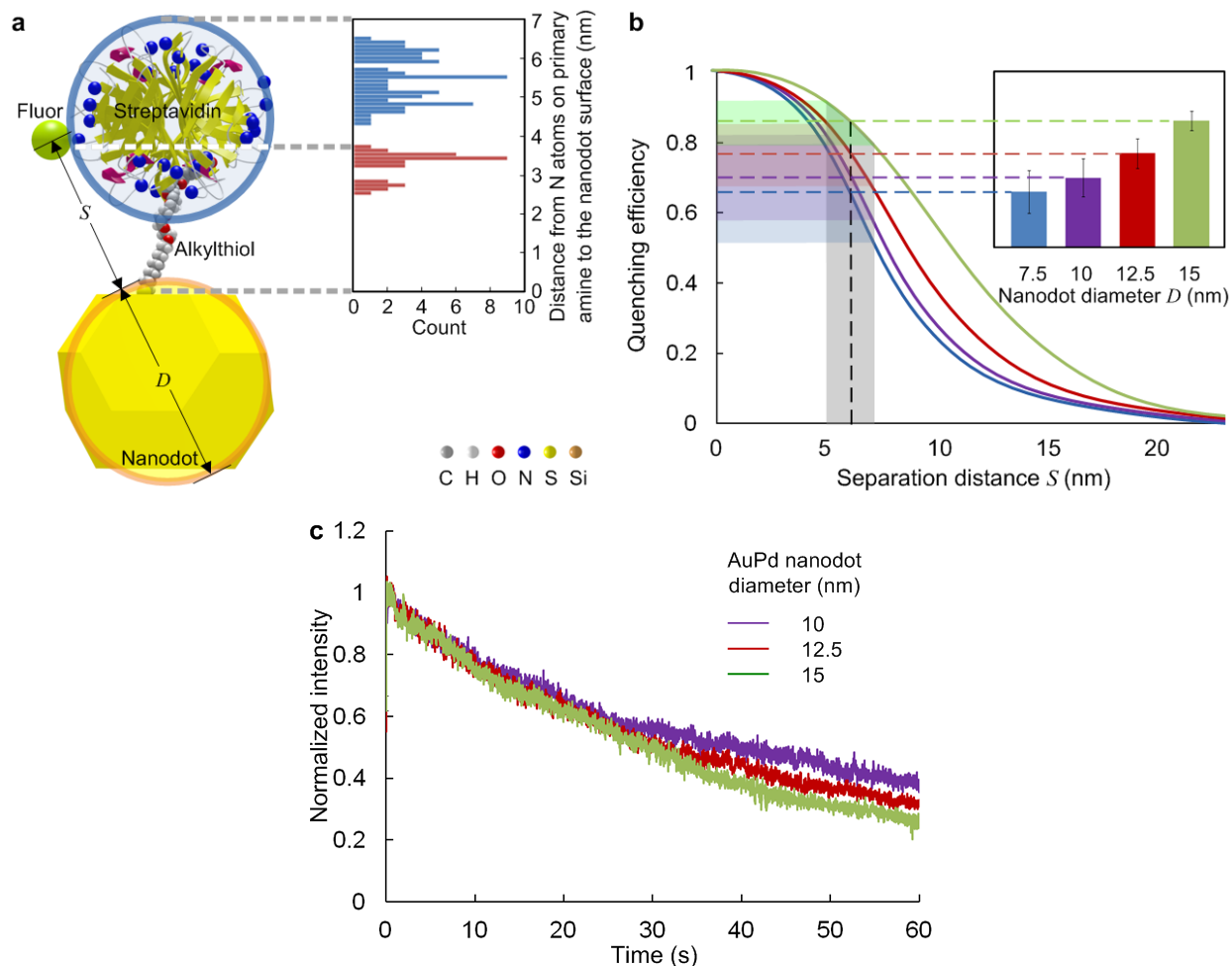


Figure 2. (a) A molecular model showing the distance distribution from the primary amines to the nanodot surface. (b) Schematic curves of quenching efficiency vs. separation distance for various nanodot size. (c) Average bleaching curves for various nanodot size.

A molecular model (Fig. 1b, 2a) was developed based on the PDB files of alkylthiol and streptavidin-biotin system<sup>4-7</sup>, and visualized by a 3D computer graphics software Blender with ePMV plugin<sup>8</sup>. The morphology of a gold nanoparticle is affected by a variety of factors including size and temperature. Because the gold nanodot was created by top-down lithography instead of synthesis, its shape is more likely thermodynamically preferred truncated octahedron<sup>9</sup> than icosahedron due to growth kinetics<sup>10</sup>. Also, the thermal annealing for the dot size of our

interest ( $\geq 5$  nm) should cause only slight modification on (111) surface area of the truncated octahedron, rather than shape transformation<sup>9,11</sup>. The alkylthiol SAM on a gold nanoparticle is quite different from the well-known  $(\sqrt{3}\times\sqrt{3})R30^\circ$  structure on the (111) bulk surface<sup>5,12</sup>. Instead, molecular dynamics simulation showed a highly asymmetric arrangement in aqueous solution at room temperature<sup>13,14</sup>.

Molecular models, as well as measurements by atomic force microscopy (AFM) or scanning tunneling microscopy (STM) indicate that streptavidin has a dimension of  $\sim 5$  nm<sup>15,16</sup>. A streptavidin-Alexa Fluor 555 Conjugate (Life Technologies) was used in this study, whose fluorophores bind to the primary amines on lysines. There are 24 - 32 lysines for each homotetramer, 6 - 8 per monomer. Fig. 2a shows the locations of the nitrogen atoms on primary amines on streptavidin. The inset shows a distance histogram from the primary amines to the nanodot surface considering all four binding sites. 69% of the distances are in the range of 4.3 - 6.6 nm. The rest are smaller, but the fluorophores are unlikely to locate there, since this would have blocked the biotin binding in the first place. In light of the fourth power dependence of quenching efficiency, this narrow distribution of distance is essential for the step size measurement, as shown in the schematic quenching curves (Fig. 2b). Compared with the work by Breshike et al.<sup>17</sup>, AuPd nanodots have less quenching than pure gold, probably because of less spectral overlap of the fluorophore emission with the nanodot surface plasmon resonance (SPR). The experimental result of quenching efficiency (inset) is obtained by normalizing step sizes with that of nonspecifically bound fluorophores on the background.

The averaged bleaching rate also shows dependence on the nanodot size (Fig. 2c). Despite bleaching, the fluorescence was kept over 90% in the first 1 s of exposure, which is used as the initial intensity. Overall, the quenching effect complicates the measurement, but also provides potential applications. For example, with a spacer of fixed distance, such as DNA instead of streptavidin, this platform can also serve as an alternative for zero mode waveguides (ZMW) to measure the quantum yield and excitation rate of single molecules<sup>18</sup>. After calibration of various distances, it can be used as a single-molecule mechanical tension sensor for membrane receptors, similar to the one developed by Stabley et al.<sup>19</sup>, but with controlled geometric arrangement.

### 3. Background noise reduction by HSQ coating

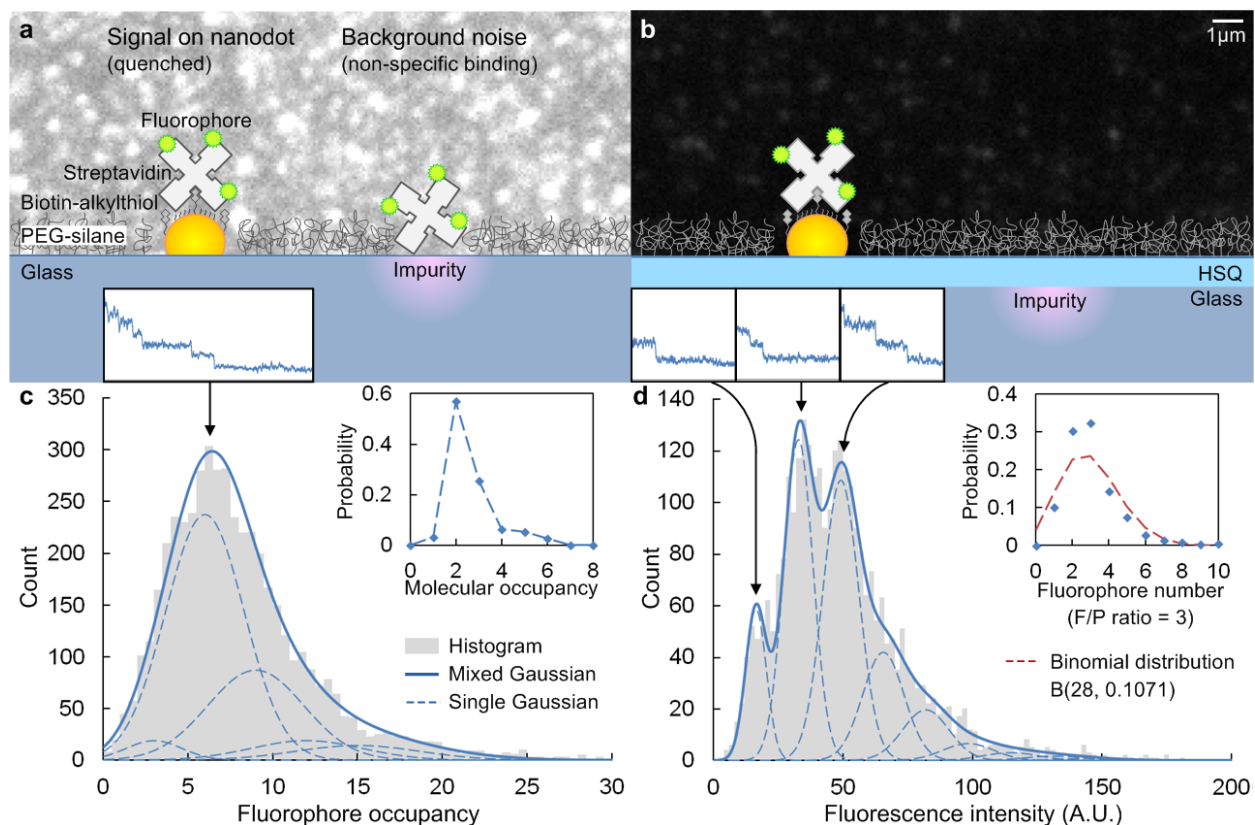


Figure 3. Schematic diagrams and fluorescence images of (a) bare glass and (b) glass with cured HSQ coating. (c) Fluorophore and molecular occupancy per spot on bare glass. (d) Fluorescence intensity and fluorophore number distribution per spot on glass with cured HSQ coating.

Schematic diagrams of glass coverslips with and without thermally cured HSQ coating are shown in Fig. 3a, b. The HSQ layer covers common impurities found on glass coverslip surface, and reduces the defects in the PEG passivation layer, resulting in a significantly reduced background fluorescence noise level. A closer look into the intensity histogram with multiple peaks reveals the probability of fluorophore number in each spot, based on a multiple Gaussian fit with a set of single Gaussians, i.e.  $n$ th convolution powers of the fitted single fluorophore intensity (bleaching step size) distribution (Fig. 3d). The insets show typical bleaching curves of single, double and triple fluorophores per spot corresponding to the first three separate peaks in the histogram. It is commonly accepted that, at low and moderate probe to protein ratios, the probe distribution follows binomial distribution<sup>20</sup>. Similarly, an average of three fluorophores

(F/P 3:1) on 28 (average of 24-32 lysines) possible binding sites of each streptavidin molecule should follow a binomial distribution  $B(28, 0.1071)$ , which is in agreement with the probability estimation (inset).

The binomial distribution of the fluorophore number per streptavidin can be approximated by a Gaussian, which was also used for a similar multiple Gaussian fit of the continuous histogram of fluorophore occupancy. It provided a better estimation of molecular occupancy than simply dividing the fluorophore occupancy by the F/P ratio. In this way, each background spot on bare glass was found to contain 2.6 streptavidins on average (Fig. 3c and inset), which indicates that the HSQ coating not only reduces the defect density, but also reduces its size to accommodate only a single streptavidin.

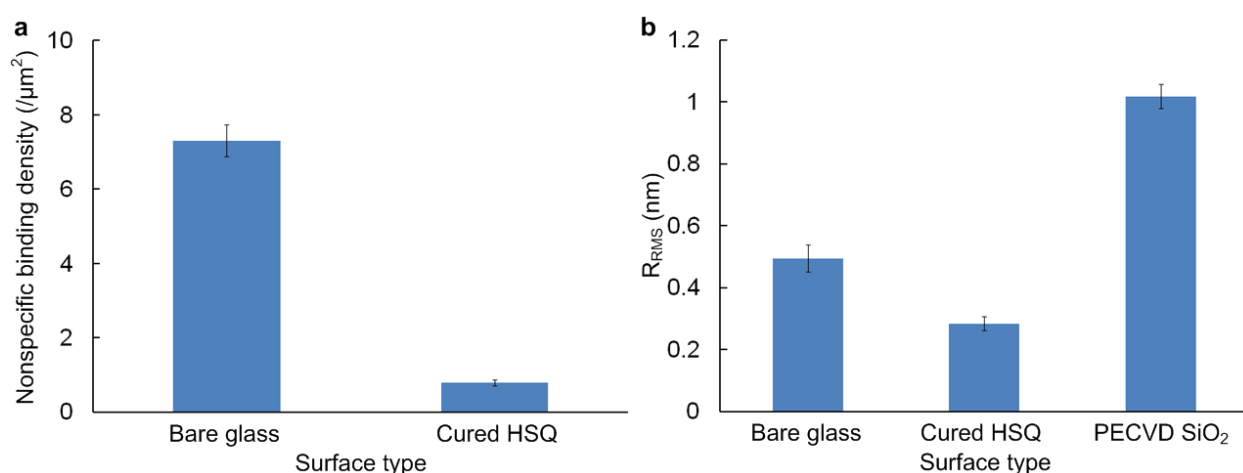


Figure 4. (a) Nonspecific bound streptavidin density on bare glass and cured HSQ surfaces. (b) Root mean square roughness of bare glass, cured HSQ and PECVD  $\text{SiO}_2$  surfaces.

A  $1600 \mu\text{m}^2$  area was imaged in five random locations on the coverslip in order to count the number of fluorescence spots. Considering the average streptavidin number per spot, the nonspecific binding density is obtained in Fig. 4a. The 15 nm cured HSQ coating reduced the streptavidin density from  $7.3 \pm 0.8$  to  $0.42 \pm 0.08$  per  $\mu\text{m}^2$ . Compared with another strategy using dichlorodimethylsilane (DDS)-Tween-20<sup>21</sup>, this density is higher, probably due to higher concentration and longer incubation time for the sake of functionalization efficiency on nanodots. But the reduction of nearly 20 folds is comparable to the latter (5 to 30 folds).

Another approach for SiO<sub>2</sub> deposition, plasma-enhanced chemical vapor deposition (PECVD, Oxford PlasmaPro NPG80), was also characterized by AFM (Fig. 4b). A 15 nm thickness was enough to form continuous film for both cured HSQ and PECVD SiO<sub>2</sub>. They were both resistant to high temperature annealing, immersion in aged piranha solution, and oxygen plasma, which are involved in the fabrication and functionalization processes. But the cured HSQ had the smallest surface roughness  $R_{\text{RMS}}$  (root mean squared), which is preferred to PECVD SiO<sub>2</sub>.

#### 4. ROI selection and spatial effect correction

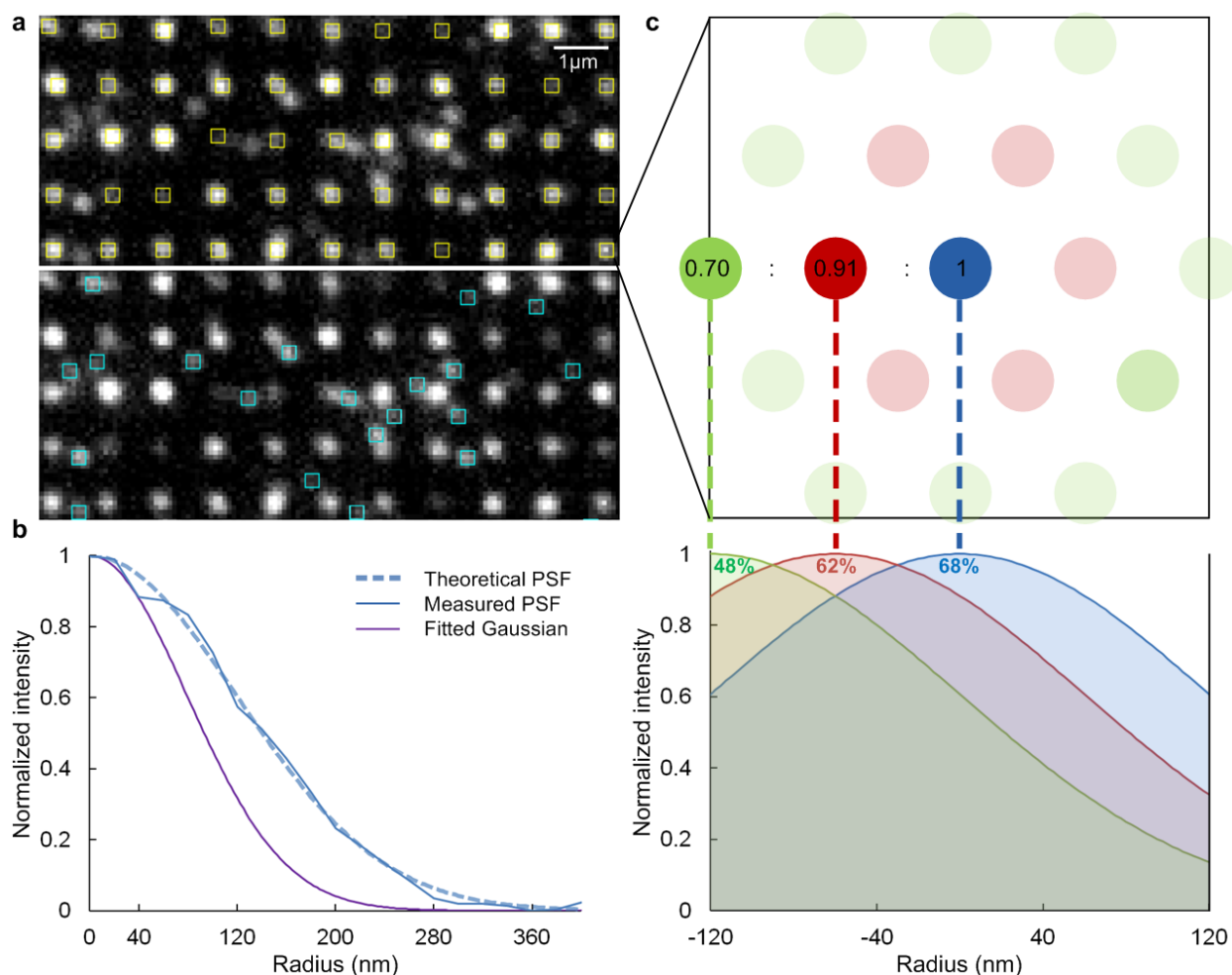


Figure 5. (a) Nanoarray fluorescence image and separate ROIs (yellow: signals of nanodot array, cyan: noises of nonspecific bound fluorophores). (b) Theoretical and measured PSFs. (c) A close-up of a 3 $\times$ 3 pixel ROI and the nanodot spatial effect on intensity. (Scale: 80nm/pixel)

A single molecule array was used to measure the point-spread function (PSF) by ImageJ using the “Mosaic” plug-in. Its fitted Gaussian has a radius (standard deviation) of 1.5 pixels (120 nm) (Fig. 5b). A 1D approximation indicates that  $\sim 68\%$  of the intensity is within a  $3\times 3$  pixel region, which is chosen as the region of interest (ROI) for the measurement of both initial intensity and bleaching step size. It not only ensures a high signal-to-background ratio (SBR), but also considers the fluctuation of PSF during bleaching.

The nanodots in each cluster are not in the same position, but in a hexagonal arrangement with 60 nm spacing. Hence, the individual positions have a spatial effect on the cluster intensity. The ROI intensity is 68% of the central nanodot, 62% of the nanodot 60 nm away, and only 47% of the nanodot 120 nm away (Fig. 5c). The resulted cluster intensity relative to the intensity of all the fluorescence in the center is listed in Table 1, based on a 1D approximation. Molecular occupancy correction coefficients for various cluster size are calculated relative to heptamer, because the step size measurement was based on heptamer arrays.

Table 1. Correction coefficients for various cluster size.

Cluster size $c$	1	2	3	4	5	6	7	10	14	19
Relative intensity in a $3\times 3$ pixel ROI	1.0000	0.9575	0.9433	0.9362	0.9320	0.9292	0.9271	0.8587	0.8131	0.7831
Correlation coefficient	0.9271	0.9683	0.9828	0.9903	0.9948	0.9978	1.0000	1.0797	1.1402	1.1839

## 5. T cell stimulation by single-molecule nanoarrays

Similarly to streptavidin-555, the bleaching step size histogram for UCHT1 Fab'-568 on 7.5 nm AuPd nanodot was fitted to a mixed Gaussian distribution (Fig. 6a). The second peak represents simultaneous bleaching events, which counts less than streptavidin, because the total number of fluorophores is much less. The F/P ratio of streptavidin was 3, while that of Fab' was only 0.45, in order to maintain the best function. This bleaching step size distribution was then used as a single Gaussian to estimate the fluorophore occupancy by multiple Gaussian fit of intensity distribution (Fig. 6b and inset). On average, there were  $3 \pm 1.8$  fluorophores per heptamer, i.e.,  $0.98 \pm 0.58$  Fab' per nanodot, close to a single molecule occupancy.



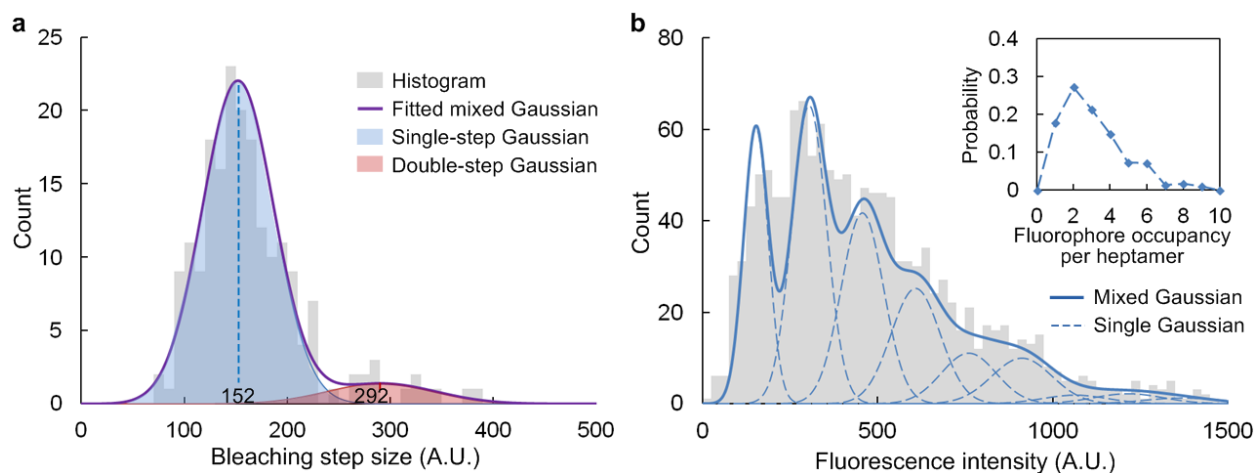


Figure 6. Histograms of UCHT1 Fab'-568 ( $D = 7.5\text{nm}$ ,  $x = 50\%$ ): (a) bleaching step size and (b) fluorescence intensity and occupancy per heptamer.

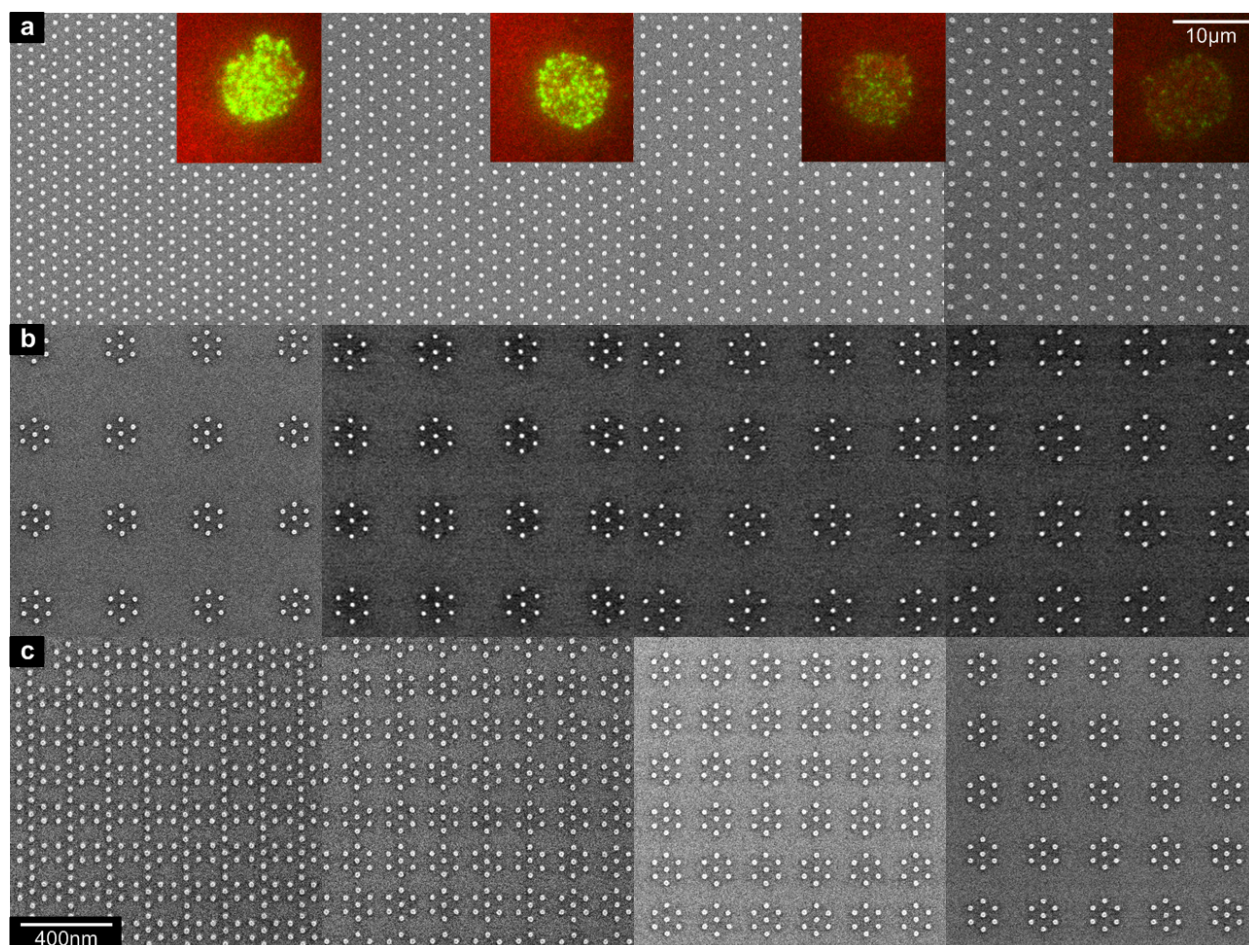


Figure 7. Various patterns on NIL mold for T cell assays: (a) hexagonal arrays with spacing 60 - 90 nm (insets are corresponding cell assay fluorescence images. green: pY-488, red: UCHT1 Fab'-568), (b)  $50/\mu\text{m}^2$  heptamer arrays with inter-dot spacing 60 - 90 nm, (c) 60 nm heptamer arrays with dot density 100 -  $250/\mu\text{m}^2$ .

Table 2. T cell activation on nanoarray of TCR binding sites.

Reference	T cell type	TCR binding ligand	Activation index	Cell assay	Adhesive or costimulatory molecule	Threshold (transition region)	Linking chemistry	Dot size	Molecular occupancy
Spatz <sup>22</sup>	Mouse CD4 <sup>+</sup>	pMHC	contact area, adhesion %, IL2 secretion	45 min, 24 hr	No	100 - 150 nm (70 / $\mu\text{m}^2$ )*	Histag, Ni-NTA thiol	NA	1.6
Spatz <sup>23</sup>	Human CD4 <sup>+</sup>	aCD3 OKT3	IL2 secretion, proliferation	17 hr, 4 days	aCD28	60 - 100 nm	Histag, Ni-NTA thiol	NA	NA
Dunlop <sup>24</sup>	Human CD4 <sup>+</sup>	aCD3 UCHT1 F(ab') <sub>2</sub>	pY intensity, cell density	5 min	ICAM-1	34 - 69 nm	Thiol	8 - 17 nm	NA
This work	Human CD4 <sup>+</sup>	aCD3 UCHT1 Fab'	pY intensity	5 min	ICAM-1	100 nm (115 / $\mu\text{m}^2$ )	Streptavidin-biotin thiol	7.5 nm	0.98

\* corrected by the molecular occupancy:  $70 \times (1.6 \pm 0.4)$ , i.e. 90 - 140 / $\mu\text{m}^2$ .

The molecular occupancy in the work by Deeg et al.<sup>22</sup> was estimated by the intensity of a 110  $\mu\text{m}^2$  hexagonal array (e.g. 35283 dots when the spacing is 60 nm) and the average intensity on a single spot. The latter was achieved by a low functionalization concentration and then assumed to be the single molecule intensity. It was a small divisor, which could cause a large measurement error. The background variation among different samples also contributed to the large variation of molecular occupancy. A few samples were only partially functionalized, and the rest ranged from single to six molecules per dot. The estimated occupancy (not single-molecule) could be used to correct the global density threshold, but is not applicable for local spacing or stoichiometry effect.

Table 3. Cell adhesion and spreading on nanoarray of integrin binding sites.

References	Cell type	Integrin binding ligand	Adhesion and spreading index	Threshold (transition region)	Linking chemistry	Dot size
Spatz <sup>25-27</sup>	MC3T3-osteoblasts B16-melanocytes REF52-fibroblasts 3T3-fibroblasts	RGD	% of spreading cells	58 - 73nm	Histag, Ni-NTA thiol	< 8 nm
Wind <sup>28</sup>	3T3-fibroblasts	RGD	% of spreading cells	60 - 80 nm	Streptavidin-biotin thiol	sub-10 nm

Single-molecule occupancy is a basic assumption in cellular studies using nanodot arrays<sup>22-31</sup>, but the tolerance depends on the dimension of the transmembrane receptors, which bind to ligands immobilized on the nanodots. For example, nanoarrays of integrin binding ligand RGD (Arg-Gly-Asp) were used to explore the geometric effect on cell adhesion and spreading. A spatial threshold of  $\sim 60$  nm was obtained in many experiments using either BCML or EBL/NIL<sup>25-28</sup> (Table 3). Because the size of an integrin head is 8 - 12 nm, any sub-10 nm nanodot can accommodate only a single integrin, even if there may be multiple RGDs occupying the nanodot. On the other hand, this assumption does not hold for smaller transmembrane molecules, like T cell receptor (TCR, a heterodimer with two  $\sim 40$  - 50 kD chains<sup>32</sup>). Molecular occupancy higher than 1 might lead to multiple TCR binding at each site, and this could alter the cellular response. This probably contributes to a great variation among different platforms<sup>22-24</sup> (Table 2).

Table 4. List of PDB files used in the molecular 3D model

Molecule	PDB file name	PDB ID
Streptavidin-biotin	Wildtype Core-Streptavidin with Biotin at 1.4A	1MK5 <sup>6</sup>
	PENTADECANE	MYS
Alkylthiol	E-AMINO BIOTINYL CAPROIC ACID	BH7
	POLYETHYLENE GLYCOL (N=34), PEG1500	15P
PEG-silane	ETHYL-TRIMETHYL-SILANE	CEQ

Table 5. Variables list

<i>c</i>	Cluster size, i.e. the number of nanodots per cluster
<i>D</i>	Diameter of nanodot (nm)
<i>d</i>	Diameter of molecule (nm)
<i>h</i>	Photobleaching step size (A. U.)
<i>I</i>	Initial intensity (A. U.)
<i>N</i>	Molecular occupancy
<i>n</i>	Sample size
<i>P</i>	Probability of a distribution
<i>p</i>	Optimal packing number
<i>r</i>	F/P ratio, i. e. the number of fluorophores per molecule
<i>S</i>	Separation distance (nm)
<i>x</i>	Mole fraction of binding ligands (%)

## References

- 1 Love, J. C., Estroff, L. A., Kriebel, J. K., Nuzzo, R. G. & Whitesides, G. M. Self-assembled monolayers of thiolates on metals as a form of nanotechnology. *Chem. Rev.* **105**, 1103-1169, doi:Doi 10.1021/Cr0300789 (2005).
- 2 Cherniavskaya, O. *et al.* Fabrication and surface chemistry of nanoscale bioarrays designed for the study of cytoskeletal protein binding interactions and their effect on cell motility. *J. Vac. Sci. Technol. B* **23**, 2972, doi:10.1116/1.2132332 (2005).
- 3 Love, J. C. *et al.* Formation and structure of self-assembled monolayers of alkanethiolates on palladium. *J. Am. Chem. Soc.* **125**, 2597-2609, doi:Doi 10.1021/Ja028692+ (2003).
- 4 Lee, J. & Kim, S. H. PDB Editor: a user-friendly Java-based Protein Data Bank file editor with a GUI. *Acta Crystallogr D* **65**, 399-402, doi:Doi 10.1107/S0907444909000451x (2009).
- 5 Latour, R. A. & Rini, C. J. Theoretical analysis of adsorption thermodynamics for hydrophobic peptide residues on SAM surfaces of varying functionality. *Journal of Biomedical Materials Research* **60**, 564-577, doi:Doi 10.1002/Jbm.10052 (2002).
- 6 Hyre, D. E. *et al.* Cooperative hydrogen bond interactions in the streptavidin-biotin system. *Protein Sci.* **15**, 459-467, doi:10.1110/ps.051970306 (2006).
- 7 Bernstein, F. C. *et al.* Protein Data Bank - Computer-Based Archival File for Macromolecular Structures. *J. Mol. Biol.* **112**, 535-542, doi:Doi 10.1016/S0022-2836(77)80200-3 (1977).
- 8 Johnson, G. T., Autin, L., Goodsell, D. S., Sanner, M. F. & Olson, A. J. ePMV Embeds Molecular Modeling into Professional Animation Software Environments. *Structure* **19**, 293-303, doi:DOI 10.1016/j.str.2010.12.023 (2011).
- 9 Barnard, A. S., Lin, X. M. & Curtiss, L. A. Equilibrium morphology of face-centered cubic gold nanoparticles > 3 nm and the shape changes induced by temperature. *J. Phys. Chem. B* **109**, 24465-24472, doi:Doi 10.1021/Jp054279n (2005).
- 10 Barnard, A. S. & Chen, Y. Kinetic modelling of the shape-dependent evolution of faceted gold nanoparticles. *J. Mater. Chem.* **21**, 12239-12245, doi:Doi 10.1039/C1jm11677k (2011).
- 11 Kuo, C. L. & Clancy, P. Melting and freezing characteristics and structural properties of supported and unsupported gold nanoclusters. *J. Phys. Chem. B* **109**, 13743-13754, doi:DOI 10.1021/jp0518862 (2005).
- 12 Ulman, A., Eilers, J. E. & Tillman, N. Packing and Molecular-Orientation of Alkanethiol Monolayers on Gold Surfaces. *Langmuir : the ACS journal of surfaces and colloids* **5**, 1147-1152, doi:Doi 10.1021/La00089a003 (1989).
- 13 Lane, J. M. D. & Grest, G. S. Spontaneous Asymmetry of Coated Spherical Nanoparticles in Solution and at Liquid-Vapor Interfaces. *Phys. Rev. Lett.* **104**, doi:ARTN 235501  
DOI 10.1103/PhysRevLett.104.235501 (2010).
- 14 Luedtke, W. D. & Landman, U. Structure and thermodynamics of self-assembled monolayers on gold nanocrystallites. *J. Phys. Chem. B* **102**, 6566-6572, doi:DOI 10.1021/jp981745i (1998).
- 15 Cooper, J. M. *et al.* The Imaging of Streptavidin and Avidin Using Scanning-Tunneling-Microscopy. *J Mater Sci-Mater El* **5**, 106-110 (1994).
- 16 Neish, C. S., Martin, I. L., Henderson, R. M. & Edwardson, J. M. Direct visualization of ligand-protein interactions using atomic force microscopy. *Br. J. Pharmacol.* **135**, 1943-1950, doi:DOI 10.1038/sj.bjp.0704660 (2002).
- 17 Breshike, C. J., Riskowski, R. A. & Strouse, G. F. Leaving Forster Resonance Energy Transfer Behind: Nanometal Surface Energy Transfer Predicts the Size-Enhanced Energy Coupling between a Metal Nanoparticle and an Emitting Dipole. *J Phys Chem C* **117**, 23942-23949, doi:Doi 10.1021/Jp407259r (2013).

- 18 Holzmeister, P. *et al.* Quantum yield and excitation rate of single molecules close to metallic nanostructures. *Nat Commun* **5**, doi:ARTN 5356

DOI 10.1038/ncomms6356 (2014).

- 19 Stabley, D. R., Jurchenko, C., Marshall, S. S. & Salaita, K. S. Visualizing mechanical tension across membrane receptors with a fluorescent sensor. *Nat. Methods* **9**, 64-U172, doi:10.1038/Nmeth.1747 (2012).
- 20 Skinner, J. P. *et al.* Introduction of the Mass Spread Function for Characterization of Protein Conjugates. *Anal. Chem.* **84**, 1172-1177, doi:DOI 10.1021/ac202239j (2012).
- 21 Hua, B. Y. *et al.* An improved surface passivation method for single-molecule studies. *Nat. Methods* **11**, 1233-+, doi:Doi 10.1038/Nmeth.3143 (2014).
- 22 Deeg, J. *et al.* T cell activation is determined by the number of presented antigens. *Nano Lett* **13**, 5619-5626, doi:10.1021/nl403266t (2013).
- 23 Matic, J., Deeg, J., Scheffold, A., Goldstein, I. & Spatz, J. P. Fine Tuning and Efficient T Cell Activation with Stimulatory aCD3 Nanoarrays. *Nano Lett.* **13**, 5090-5097, doi:Doi 10.1021/Nl4022623 (2013).
- 24 Delcassian, D. *et al.* Nanoscale Ligand Spacing Influences Receptor Triggering in T Cells and NK Cells. *Nano Lett.* **13**, 5608-5614, doi:Doi 10.1021/Nl403252x (2013).
- 25 Arnold, M. *et al.* Activation of integrin function by nanopatterned adhesive interfaces. *Chemphyschem* **5**, 383-388, doi:DOI 10.1002/cphc.200301014 (2004).
- 26 Cavalcanti-Adam, E. A. *et al.* Cell spreading and focal adhesion dynamics are regulated by spacing of integrin ligands. *Biophys. J.* **92**, 2964-2974, doi:DOI 10.1529/biophysj.106.089730 (2007).
- 27 Huang, J. H. *et al.* Impact of Order and Disorder in RGD Nanopatterns on Cell Adhesion. *Nano Lett.* **9**, 1111-1116, doi:Doi 10.1021/Nl803548b (2009).
- 28 Schwartzman, M. *et al.* Nanolithographic control of the spatial organization of cellular adhesion receptors at the single-molecule level. *Nano Lett* **11**, 1306-1312, doi:10.1021/nl104378f (2011).
- 29 Cai, H. *et al.* Bifunctional nanoarrays for probing the immune response at the single-molecule level. *Journal of vacuum science and technology. B, Nanotechnology & microelectronics : materials, processing, measurement, & phenomena : JVST B* **31**, 6F902, doi:10.1116/1.4823764 (2013).
- 30 Jaehrling, S., Thelen, K., Wolfram, T. & Pollerberg, G. E. Nanopatterns Biofunctionalized with Cell Adhesion Molecule DM-GRASP Offered as Cell Substrate: Spacing Determines Attachment and Differentiation of Neurons. *Nano Lett.* **9**, 4115-4121, doi:DOI 10.1021/nl9023325 (2009).
- 31 Ranzinger, J. *et al.* Nanoscale Arrangement of Apoptotic Ligands Reveals a Demand for a Minimal Lateral Distance for Efficient Death Receptor Activation. *Nano Lett.* **9**, 4240-4245, doi:DOI 10.1021/nl902429b (2009).
- 32 Weiss, A. Structure and Function of the T-Cell Antigen Receptor. *J. Clin. Invest.* **86**, 1015-1022, doi:Doi 10.1172/Jci114803 (1990).